Physical and Digital methods for tunable metasurfaces

James Eric Michael Whitehead

A dissertation submitted in partial fulfilment of the requirements for the degree of

Doctor of Philosophy

University of Washington

2022

Reading Committee:

Arka Majumdar, Chair

Igor Novosselov, GSR

Manjeri Anantram, Member

Karl Bohringer, Member

Program Authorized to Offer Degree:

Department of Electrical and Computer Engineering

Table of Contents

1. Introduction

Optics are used in our everyday life. We use them in things like video conferencing, unlocking your phone, snapping a picture, while driving to illuminate the road, and using the internet. This is a large and diverse industry where small performance improvements can provide meaningful results.

Metasurfaces are a growing field in optics which can be appealing in select applications. Metasurfaces are 2D arrangements of sub-wavelength optical scatterers that can perform many of the existing optical functions as conventional optics. However, they potentially have several advantages such as price, performance, or flexibility. Many optical systems require complex, non-scalable fabrication techniques such as diamond milling, lapping, and coating which makes these devices extremely expensive[1].

Metasurfaces belong to a larger class of diffractive optics. Conventional diffractive gratings are composed of structures that have periodicity on the order of several wavelengths, exposing the wave-like nature of light. This can be used to produce diffraction and dispersion for many practical applications. These include lensing, beam splitters, holograms, Fourier domain operations, anomalous refraction, color splitting, and wavelength selective tunable mirrors. In some of these applications under certain conditions, there can exist areas where higher order diffraction from the grating is undesirable. Multiple diffraction order will negatively impact the efficiency of a lens and produce multiple overlapping images where the modes overlap.

To address this issue, the period of the grating can be reduced to the point where there is no longer has any non-zero order diffraction. In this regime, a term that has become popular is called a metasurface or sub-wavelength grating. The metasurface is made up of large array of individual scatterer, periodically arranged in one or two dimensions. Each scatterer will perturb the wavefront as it propagates though the surface, imparting a phase delay and intensity modulation to the wavefront. The design of the scatterer is important since scatterers can properties ranging from near unity reflection to complete transmission. This can increase design flexibility since the surface can be designed to be completely reflective, completely transmission, or something in-between. These properties can also vary across the surface leading to multi-functional optics.

In optics, the scatterer properties cannot be generally simulated with ray optics, or even wave optics. At these scales, intuitions about reflections and refraction break down with permittivity distributions that change rapidly long with counterpropagating waves, complex boundary conditions, and scattering. While rigorously derived scattering behavior of many geometries can been derived[2], general purpose rigorous grid and mesh based solvers exist that can determine the scattering properties of arbitrary scattering elements.

Much like how the interaction between light and individual atoms can be modeled and used to inform effective bulk material properties[3], modeling the interaction of light with individual scatterers can give large scale effective optical properties of an effective material. This effective material is composed of the individual elements or meta-atoms, creating an effective "meta" material. By adjusting the

scatterer geometry, the effective index of the meta-atoms can be adjusted, which them impart a custom response on a wavefront. The thin layer or meta-atoms can be modeled as a thin layer of phase delay and intensity modulation, leading to anomalous refraction and reflection.

Using this arbitrary spatial phase delay and intensity attenuation, all manner of optics can be produced. Lensing, for example, is an action that can be performed with simple phase shifts across a plane. A spatial gradient in phase will cause an anomalous refraction to occur, affecting the deflection in a ray that would not be present if the interface was smooth. By building phase profile sufficient to deflect rays according to a lensing requirement, a lens made with a flat surface can be produced. More generally, using various design methods, an arbitrary intensity distribution can be created by building up appropriate phase delays so that at a desired plane, light with interfere to produce the designed image. These design methods can span from analytical methods to various computational approaches discussed later in this thesis. In some cases, it is necessary to include the fabrication characteristics and imperfections in the design method to achieve better results.

Fabrication of meta-optics is a complex process requiring advanced tools and system. Due to the scale required, the available tools must be able to define features that are on the order of a wavelength of light. For blue light, this means a wavelength of 450nm. This scale is hard to achieve using most fabrication methods. However, in the field of semiconductor electronics, these scales have been produced in devices consistently for many years, and the tools produced for this large industry are readily available at reasonable costs due the immense scale of the

semiconductor industry. In addition, while tool time and per wafer costs can be high, the parallelism of established wafer production allows for low per unit costs. Wafer processing uses a large thin disk of material to define many devices on its surface. Every process performed on the wafer is performed on all devices on the wafer, allowing for sharing of the overhead to process a wafer. Large scale fabrication of meta-optics is relatively trivial in comparison to existing semiconductor production[4], leading to low unit cost at large scales. Existing semiconductor technologies must achieve feature sizes much smaller than required for meta-topics and require more steps. Semiconductor manufacturing can require tens of layers, each requiring a lithography step followed by a deposition, removal, implantation, thermal processing, or chemical processing. Comparatively, most passive meta-optics in literature have a maximum of one lithography step. This reduction in complexity can reduce cost significantly as defects in the processes do not compound. Semiconductor industry materials have also been well established, such as silicon, silicon oxide, and silicon nitride. Single crystal silicon wafers, useful for their optical quality and transparency in near infra-red wavelengths, are produced at very large scales, leading to low unit costs. Tools are readily available that are capable of etching as depositing thin silicon layers. Similarly with silicon oxide, it is a commonly used material in optics, along with its numerous composite glass mixtures, is available in wafer form with various bulk grades, defect concentrations, and surface finishes. Finally, silicon nitride, a high refractive index ceramic with potential for low optical losses, has gain maturity as integrated circuit insulators, dielectrics, and passivation layer. Thus, tools are available that can

deposit high quality films suitable for optical applications at relatively high deposition rates. Other materials can also be deposited through various other means. Sputtering can deposit a variety of material, including alloys, compounds, and even polymers. Gasses can be used during sputtering to incorporate other compounds in the final film or form reaction byproducts on the surface. This can be useful when depositing metal oxides and nitrides since the sputter target, or source, can be made up a higher thermal and electrical conductivity metal. When the desired deposition material isn't prone to decomposition before its vaporization temperature, evaporation is a practical method to producing thin films. A material is heated in a high vacuum and the material particles, unincumbered by an atmosphere, will transfer through space until it impacts the desired device to be coated. The high vacuum atmosphere also reduces the prevalence of reaction of these high energy particles. Other methods that can be used to deposit various other substances involve various chemical reactions, known as chemical vapor deposition. A vast number atomic layer deposition chemistries are available that can conformally coat few atomic layer films. Furthermore, more general chemical deposition can be used to deposit bulk films by precipitation reaction products on the surfaces of devices using pressure and temperature controlled chemical reactors, commonly assisted with microwave induced plasma to tune the reaction.

These deposition techniques open up a huge number of optical material systems, allowing for choices in terms of bulk material absorption, scattering, refractive index, mechanical strength, chemical compatibility, and ease of processing.

Finally, meta-optics allow for novel and combined optical operations such as polarization[5] and wavelength multiplexed[6] focusing. The transmission characteristics of a meta-optic scatterer can be tuned to perform arbitrary polarization transforms, allowing for the creation of waveplates and polarizers. On a single device with the same processing, various distinct polarization modifications can be performed across in different parts of the device based off the shape or the scatterer. Extra degree of freedom provides additional flexibility in design[7].

Monolithic integration of meta-optics with light emitters[8] like LEDs and lasers remove costly requirements of alignment to optics further down the line, and reduces alignment variation in completed parts. Meta-optics can be lithographically defined using the same processes used in the fabrication of the light sources themselves. Discrete photodiodes and arrays[9] can also benefit from direct integration.

Computational optics[10] using arbitrary phase profiles can also be easily realized without the higher order power loss of diffraction gratings. Thanks to its low mass, meta-optics can also be fabricated on Micro-Electro Mechanical System (MEMS) for active alignment or tuning[11]–[13].

Despite these advantages, it is important to emphasize the limitations of meta-optics. With a few rare exceptions, published examples of metasurfaces generally have poor efficiency[14], [15] when compared to coated refractive optics. While this may be surmountable issue with design and fabrication that will resolve itself, it should be noted.

More importantly however, the optical scatterers that make up the metasurfaces have strong chromatic dispersion[16]. Depending on the structure, this dispersion can be slow and predictable or quickly varying with many resonances. This makes designing metasurfaces that cover a large bandwidth of light problematic. This excludes high efficiency, broadband metasurface imaging. In low bandwidth imaging, the dispersion of scatterers can be tuned[17], given enough degrees of freedom in the scatterer geometry. The fabrication tolerance will also be an issue for the feature size and complexity required for visible scatterer designs but can be applied at longer wavelengths. Discontinuities in phase can be limiting in large aperture meta-optics where the phase gradient far from the center becomes too large to be represented with the scatterer grid.

Despite these limitations, there are many potential applications of meta-optics. There are many fields where a single, narrowband, or few discrete wavelengths are used. Since their development, LEDs and Lasers have become ubiquitous in industry and consumer electronics. These narrowband sources, in many cases, must be used in conjunction with optics for light collection and control. Smartphones will use infra-red optics to determine the shape of their user's face. Cars use time-of-flight systems to determine the distance of surrounding obstructions to prevent collisions. 3D scanners are used to import geometries for rapid design at incredible accuracies and impressive scales. Laser systems are used in industrial cutting and welding to manufacture parts that have higher complexity and achieve throughputs than otherwise unachievable. The medical field uses narrowband light to excite and detect fluorescent molecules in living organisms[18] and image inside of the body.

All these systems require accompanying optics to achieve good performance. In many of these cases, meta-optics may be able to perform better than existing solutions. The work presented here is only a small look into field of meta-optics.

I believe the topics covered in this thesis highlight the strengths of meta-optics. The versatility of meta-optics allows us to achieve extended depth of focus images used in digital focusing and electrical tuning of scatterers for narrow bandwidth spatial light modulation using highly reflective scatterer cavities. In addition, computational meta-optics are demonstrated by performing complex optical 1D-to-2D transforms.

2. Metasurface Optics

Metasurfaces are 2D arrangements of subwavelength optical scatterers. By placing these scatters at a pitch that is below an order of a wavelength of light, these structures do not inherently diffract light into higher orders. Variations in the scatterer geometry and orientation are used to modify an incoming wavefront. Metasurfaces can delay and attenuate different polarizations of light to perform various optical operations, as governed by the generalized grating equation[19]:

$$n_m \sin(\theta_m) = n_i \sin(\theta_i) + \frac{m\lambda}{d}$$

This equation for the diffraction of light through a grating is shown here where n_m is the refractive index medium that the diffracted order is entering, θ_m is the angle that the output order will diffract, n_i is the refractive index of the incident medium, θ_i is the angle of the incident light, m is an integer corresponding the a mode order, λ is the free space wavelength of light, and d is the period of the grating.

For a specific range of incident angles, medium refractive indices, and wavelength a period can be derived that will not diffract into non-zero order modes. For example, for a grating surrounded by index 1 material on both sides, a periodic grating with a period smaller than of $\frac{\lambda}{2}$ will not have any non-zero order diffraction, regardless of the input angle. Also, if there is only normal incident light, a grating with a period below λ will have no non-zero order diffraction. This sets the acceptable range of scatterer periods to be no greater than λ and if arbitrary incident angles are present, then the period should be no greater than $\frac{\lambda}{2}$.

An appropriate scatterer period is determined using the previous equation, in order to only have non-zero order diffraction. However, when the scatter geometry to made to vary across the substrate, the phase delay at the interface will vary causing refraction at angles that are not defined by Snell's law. An addition term can be added to Snell's law to encompass the phase gradient to form the generalized Snell's Law[20]. This anomalous refraction of light at an interface with spatially varying phase delay can be represented using the equation below:

$$\sin(\theta_t)\, n_t = \sin(\theta_i)\, n_i + \frac{\lambda_0}{2\pi}\frac{d\phi}{dx}$$

Here, θ_i and n_i are the incident angle and refractive index of the incident ray respectively while θ_t and n_t are the angle and refractive index of the transmitted ray. λ_0 is the free space wavelength leaving the phase term ϕ and distance term x. For a phase profile with a constant phase delay at the interface, this means the generalized refraction equation simplified to just Snell's law. By designing a phase profile with the appropriate phase distribution, rays can be redirected with large degrees of freedom.

This spatially varying phase can be physically represented by the meta-optics scatterers. At optical wavelengths, there are commonly of two material systems used: metallic or dielectric. For metallic meta-optics, simple designs can model the scatterers as simple plasmonic resonator. By adjusting the shape of the resonators, the phase and intensity of light after interaction can be modified. These devices are relatively easy to fabricate[21] since they typically involve a single metal deposition and lithography stage but suffer from poor efficiency at visible

wavelengths due to metal's high intrinsic loss. The other method to create metasurfaces uses dielectric scatterers. Dielectrics such as titanium oxide (n=2.5), aluminum oxide (n=1.7), and silicon nitride (n=2) and silicon are commonly used due to their low loss and high refractive index in visible wavelengths along with availability in standard microchip fabrication processes. Regardless of the type of metasurface used, they both benefit from a single stage lithography process which is important for fabrication scalability.
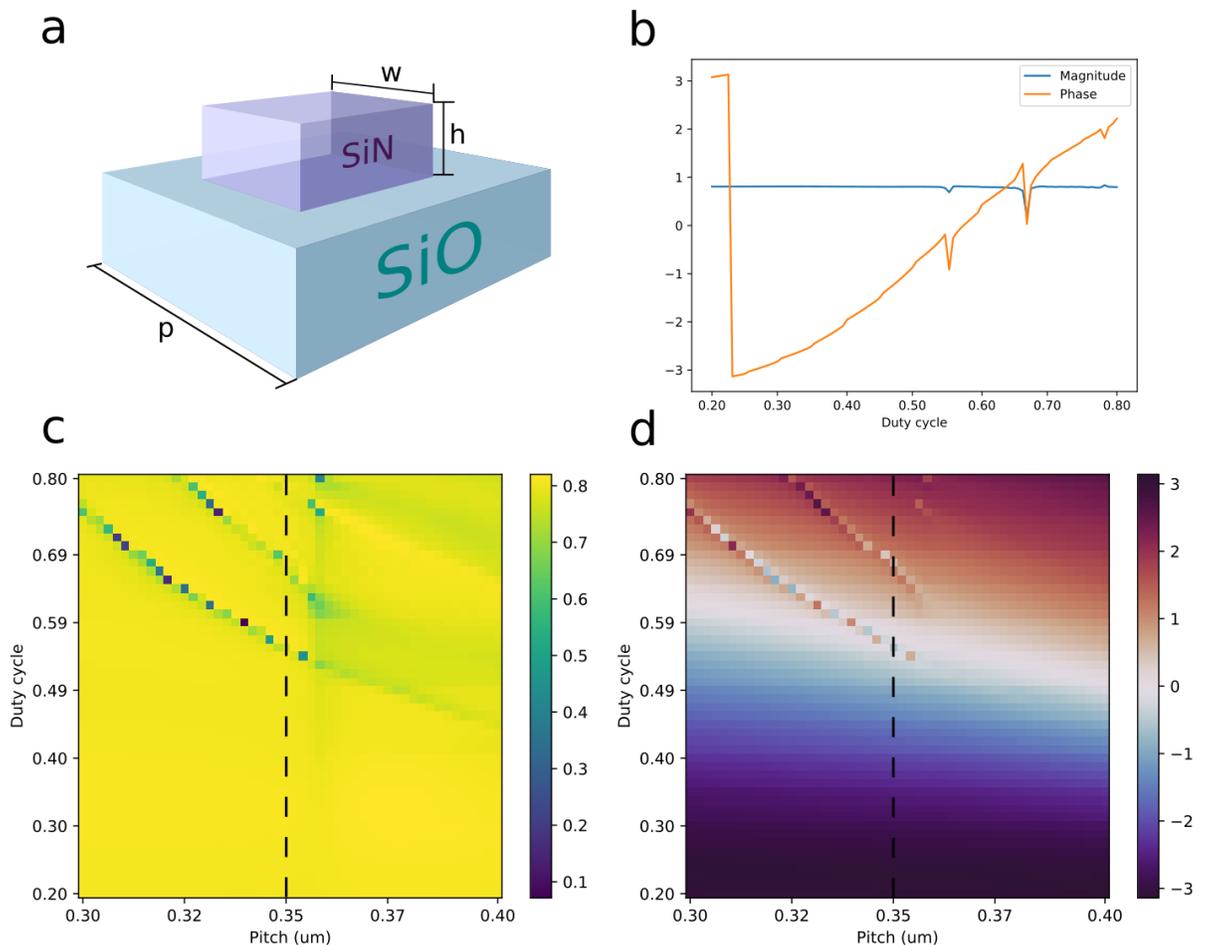
Fig. 2.1- For 633nm thick silicon nitride posts on a silicon oxide substrate. a) Geometry of the scatterer. W is the width of the

square post, h is the thickness of the silicon nitride layer. b)

Magnitude and phase of a plane wave input for posts with 350nm

period. c) Intensity of transmitted light through the unit cell. d)

Phase angle of transmitted light through unit cell in radians [22]
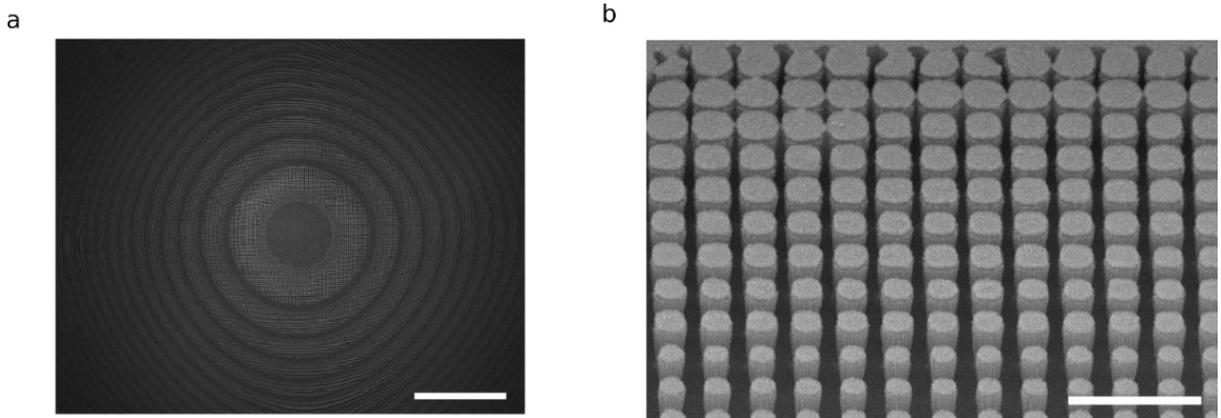
Fig. 2.2 - SEMs of the fabricated device structure. The metasurface was sputter

coated with gold-palladium alloy for charge dissipation a) Scale bar is 100um. b)

Scale bar of 1um taken at 45 degrees to normal. [22]

Metasurfaces made of silicon nitride scatterers on dielectric substrates have the advantage of CMOS process compatibility and low loss at visible wavelengths[4]. Regular square lattices are used to arrange the scatterers. While non-periodic metasurface have been shown[23], they add additional complexity to the design and simulation.

Easily fabricable structures using scalable semiconductor fabrication techniques place various constrains on the practical geometries. Since these structures are fabricated with standard, single step, binary lithography, the scatterer height must

remain constant. Also, many methods work well with constant cross-section structures.

To reduce the sensitivity of the device to fabrication imperfections, a scatterer height and lattice constant that produces slowly varying transmission characteristics is chosen. Also, high transmission is favored to maximize the efficiency of the device.

The geometries are simulated using standard rigorous electro-magnetic wave based computational techniques such as Finite Difference Time domain[24] and Rigorous Coupled wave analysis[25]. In most cases, each unit cell's transmission characteristic is calculated in a periodic simulation.

3. Design and fabrication of Meta-optics

Sections are adapted, with permission, from *Fast extended depth of focus meta-optics for varifocal functionality* James E. M. Whitehead, Alan Zhan, Shane Colburn, Luocheng Huang, and Arka Majumdar [22].

3.1. Design

Once an appropriate design of scatter has been found, these scatterers can then be used to implement various spatially varying phase profiles. One such phase profile is a lens or, more specifically, a hyperbolic phase profile. While lenses are usually much thicker than a wavelength of light, their behavior can be realized using a sub-wavelength thickness metasurface. This is useful when the thickness of the lens is a constraining factor such as in portable and compound optics.

$$\phi(x, \ y) = k\left(\sqrt{x^2 + y^2 + f^2} - f\right)$$

The phase profile that implements a simple lens is described here, where k is the wavenumber (magnitude of the propagation vector), x and y are the Cartesian coordinates in the plane of the lens, and f is its focal length. By mapping the desired phase shift to the database of simulated geometries, a spatially varying phase profile that causes lensing is made.

This method does not only apply to simple lenses. In fact, arbitrary phase profiles can be fabricated to perform complex operations. Here [26], an Alvarez phase profiles (a phase profile used in varifocal imaging) is created by mapping the desired phase to the scatterer geometry.

In addition, metasurfaces are not simply restricted to only phase shifts. The scatterers can have strong polarization and wavelength sensitivity so they can be used to change the wavefront in a variety of ways. In this work[7], multi-chromatic light is split into 6 different focal spots based on the color and polarization. This device is meant to beat attenuative filtering mechanisms (such as dyes and polarizers) since the light is not absorbed on before each pixel but redirected leading to higher efficiency cameras.

Finally, through inverse design of phase masks, complex operations like linear image classification can be performed like in this paper[27]. Here, hand-written images can be classified using cascaded metasurfaces.

Moreover, many different optical functions can be realized using these methods. However, most design methods are limited when the phase changes too quickly.

When simulating the transmission characteristics, we assume that the neighboring pillars have a similar shape. This is called the local phase approximation. Local phase approximation becomes important when the inter-pillar coupling becomes significant which has been shown to occur when the pillar materials have poor field confinement[28]. Poor field confinement tends to occur when the index contrast is small, such as in the silicon nitride metasurface that we make.

When the local phase approximation breaks down, other more complex design methods are required like those seen in this paper[29]. Here, a differentiable function is generated that maps parameters of pillar geometry and nearest neighbor pillar geometries to the central pillar's near-field transmission. This allows for

iterative gradient descent algorithms to be applied to the geometries to optimize some aspect of the generated near-field.

3.2. Angular spectrum

When a single component of polarized light propagates through free space in the far-field, it can be treated as a superposition of scalar waves[30]. An efficient way of modelling the propagation of scalar waves is through free space is the Angular Spectrum method. This method allows for fast calculation of fields on planes displaced from the source plane since due to efficient algorithms to calculate 2D discrete Fourier transform. This beats the complexity and speed of methods like Rayleigh-Sommerfeld diffraction which requires $O(N) = N^4$ to propagate over a $N \times N$ output plane. However, the angular spectrum is limited to parallel planes which may be limiting in various circumstances. When the field and at only few points in space is required or across planes that are not parallel to the source plane, the Raleigh-Sommerfeld propagation method can be significantly faster.

In some cases, particularly when performing the gradient descent operation while using discrete sampling of the function, aliasing of the field leads to optimization of fields that are non-physical. To address this, an anti-aliasing filter should be used [31]

3.3. Metasurface fabrication

The fabrication of silicon nitride visible metasurfaces specific to my research

proceed as follows.
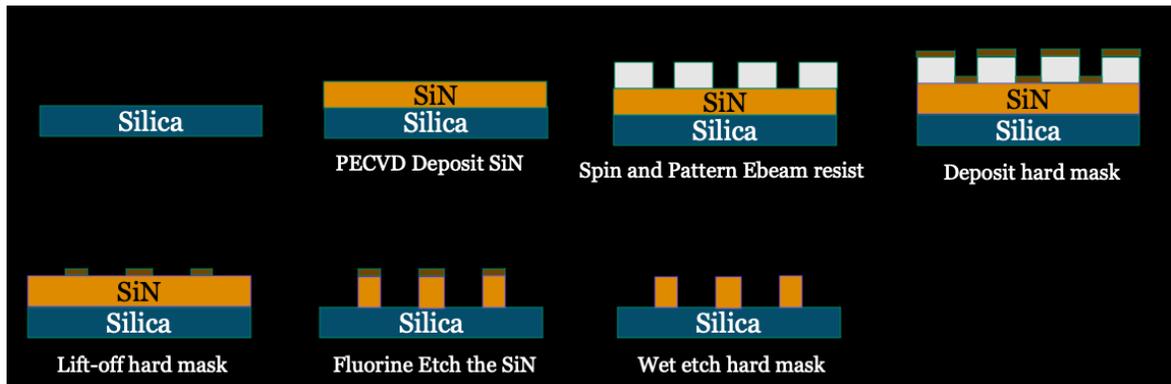
Figure 3.1. Fabrication process flow for silicon nitride metasurface

A double side polished fused silica wafer is cleaned in a hot solution of sulfuric

acid and hydrogen peroxide for 10 minutes. Plasma-enhanced chemical vapor

deposition is used to build a 633 nm layer of silicon nitride on one side. A layer of

200 nm of ZEP-520A positive tone electron beam resist is spun after a short clean

in oxygen plasma to maximize adhesion. An estimated 8 nm of Au/Pd is sputtered

to dissipate charge produced from the electron beam. The pattern is written using

electron-beam lithography (JEOL JBX6300FS at 100 kV). The Au/Pd layer is

removed by immersing in Transene gold etchant Type TFA with mild agitation.

The resist is developed in Amyl acetate and rinsed in Isopropyl alcohol. The wafer

is descumbed using a weak oxygen plasma. A layer of 50nm of nickel with 5nm

chromium adhesion layer is deposited using an electron beam evaporator. The

metal is selectively removed by dissolving the supporting resist in a solvent while

sonicating. An inductively coupled fluorine plasma etcher (Oxford Plasmalab 100)

etched the Silicon nitride layer down to the substrate. The metal hard mask is removed with nickel and chromium etchants. The wafer is cleaned using a hot solution of sulfuric acid and hydrogen peroxide for 10 minutes. Using direct write photolithography and electron beam evaporation, a chromium aperture is made to block stray light from bypassing the metasurface.

4. Extended depth of focus (EDOF)

This section is adapted, with permission, from *Fast extended depth of focus meta-optics for varifocal functionality* James E. M. Whitehead, Alan Zhan, Shane Colburn, Luocheng Huang, and Arka Majumdar [22].

Extended depth of focus (EDOF) optics can enable lower complexity optical imaging systems when compared to active focusing solutions. With existing EDOF optics, however, it is difficult to achieve high resolution and high collection efficiency simultaneously. The subwavelength spacing of scatterers in a meta-optic enables the engineering of very steep phase gradients; thus, meta-optics can achieve both a large physical aperture and a high numerical aperture. Here, we demonstrate a fast (f/1.75) EDOF meta-optic operating at visible wavelengths, with an aperture of 2 mm and focal range from 3.5 mm to 14.5 mm (286 diopters to 69 diopters), which is a 250× elongation of the depth of focus relative to a standard lens. Depth-independent performance is shown by imaging at a range of finite conjugates, with a minimum spatial resolution of ~9.84 μm (50.8 cycles/mm). We also demonstrate operation of a directly integrated EDOF meta-optic camera module to evaluate imaging at multiple object distances, a functionality which would otherwise require a varifocal lens.

Optical imaging systems operating at finite conjugates suffer from a limited depth of focus. This often necessitates complex refocusing mechanisms. While large scale optics can be refocused by manually translating individual elements, integrated applications require high precision actuators and active feedback to modify the optics. Several active solutions are currently used to adjust the focal plane in

integrated systems such as electro-wetting[32] and MEMS actuation[11], [13]. These solutions, however, have various drawbacks such as delicate control mechanisms, extra electrical circuitry, multiple acquisitions, and temperature sensitivity. Instead of dynamically changing the focal plane, a static optic with an extended focal plane can be used to image all objects in a desired depth covered by the focal range [33]. For conventional lenses, the depth of focus is inversely proportional to the square of the numerical aperture $\left(NA \sim \frac{D}{2f}\right)$ where D is the diameter, and f is the focal length of the lens. This leads to a trade-off between the depth of focus and resolution. The depth of focus of any lens can be increased by reducing the NA but that limits the achievable resolution of the optical system due to the diffraction limit. Additionally, for any practical applications, we need a sufficiently large diameter lens to ensure we can collect enough photons to achieve an acceptable signal-to-noise ratio.

Extended depth of focus (EDOF) refractive lenses have been demonstrated in the past exploiting wavefront coding[33]–[35]. With the need for miniaturizing imaging systems for emerging applications like autonomous navigation, smart home, and the Internet of Things, there is a growing trend of migrating from refractive elements to flat diffractive optics. Unsurprisingly, EDOF concepts have also been demonstrated in diffractive optics in the recent past. Specifically, exploiting inverse design, an extreme depth of field for an EDOF lens was reported using multi-level diffractive optics[36]. The reported 1.8mm EDOF lens had a smallest focal length of 5 mm, with the maximum NA being 0.16.

Thanks to their sub-wavelength periodicity, meta-optics are capable of supporting higher phase gradient and thus larger NA, compared to multi-level diffractive optics. Meta-optics are sub-wavelength diffractive optics, which can guide all the light to the zero-th order and can provide a full 2π phase-shift using a binary mask [37], [38], making them compatible with single stage lithography process. EDOF meta-optics have previously been utilized to mitigate chromatic aberrations in meta-optics [10], [39]. Recently, inverse design techniques have also been used to create EDOF meta-optics[40]; however, the utility of EDOF meta-optics for finite conjugate imaging at different object and image distances has not been demonstrated. In this work, we report a 2 mm diameter EDOF meta-optics with a maximum numerical aperture of 0.28 ($f/\# = 1.75$). The extended depth of focus is 11 mm (from 3.5 mm to 14.5 mm), and thus the optical power in this system can be changed from 69 diopter to 286 diopter. We note that for a standard hyperboloid lens with a focal length at the center of the above range, the depth focus is expected to be $\sim 4\lambda \left(\frac{f}{D}\right)^2 \approx 43\mu m$ for green light. Thus, our EDOF meta-optics shows $250 \times$ elongation of the depth of focus compared to a standard lens. We also demonstrate imaging in multiple finite conjugate planes, where the required focal length changes from 3.65 mm to 7.55 mm and observed a resolution of $\sim 8\mu m$ in the object plane. Finally, we report direct integration of meta-optics onto a commercial camera module and show imaging at different object planes. Thus, exploiting a static meta-optics and computational backend, we can implement the functionality of a varifocal lens. Transferring such hardware functionality to the software, termed here as digital tuning, could usher into a new era of "software defined optics".

There are several different types of EDOF meta-optics reported in the literature before[39]. Here, we employ a cubic EDOF[10], with a phase profile

$$\phi(x,y) = \frac{2\pi}{\lambda}\left(\sqrt{x^2 + y^2 + f^2} - f\right) + \frac{\alpha}{R^3}(x^3 + y^3)$$

Here, λ is the operating wavelength, x and y are the cartesian coordinates, f is the nominal focal length of the lens, R is the radius of the phase mask, and α determines the strength of the cubic component. For our meta-optic, we set α to be 100π, R is $1\,mm$, and f is $5.6\,mm$. We used silicon nitride (SiN) pillars on quartz as the scatterers for the meta-optics (Fig. 4.1a). For the scatterers, we used square posts to ensure polarization-insensitive operation, large phase coverage for a given height as well as faster writing speed in electron-beam lithography. We simulate the transmission characteristics of these square posts using Lumerical FDTD Solutions under periodic boundary conditions to ensure we have high transmission while covering the whole $0 - 2\pi$ phase-shift (Fig. 4.1b). The meta-optic is then created by mapping the desired phase to the appropriate scatterer geometry under the local phase approximation[38], [41]. A cubic meta-optics do not produce a lens-like point spread function (PSF), and to extract the depth of focus, we calculate the correlation of the PSF along the optical axis[39] (Fig. 4.1e). We define the depth of focus as the range where the correlation value stays above 0.5. From the numerical analysis, we estimate the depth of focus to be 11 mm, with a minimum focal length of 3.5 mm. This makes the maximum numerical aperture of the lens 0.28. Figs. 4.1c and

4.1d show the simulated PSF of the cubic EDOF at the minimum and maximum

focal distances.
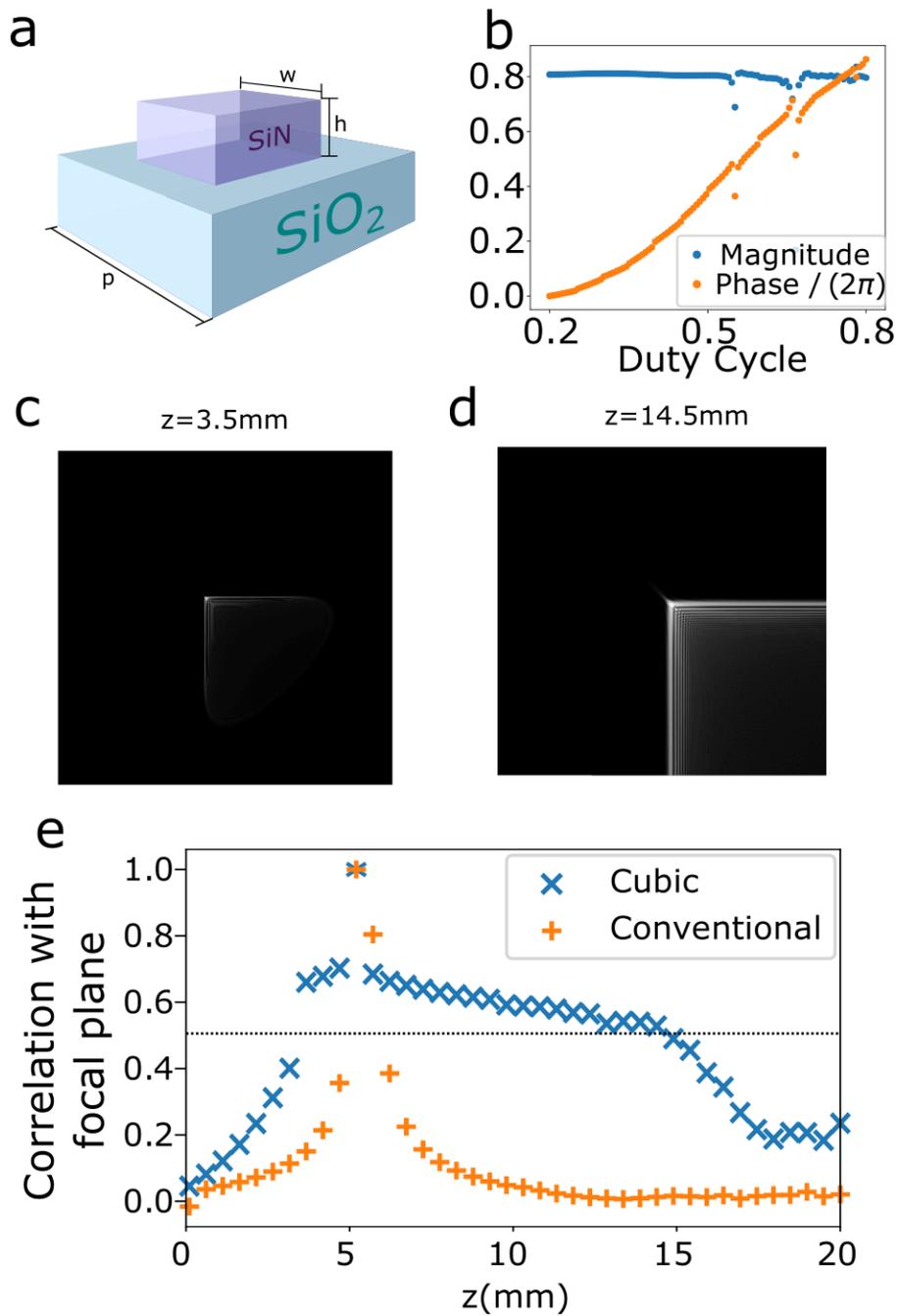
Fig. 4.1. Scatterer and meta-optics design and simulation: a)

Schematic of $h = 633nm$ thick SiN square posts on a silicon oxide

substrate. The periodicity p is kept constant, and the width w is

changed to cover the whole $0 - 2\pi$ phase. b) Magnitude and phase

of the transmitted light for a plane wave input with $p = 350nm$. c)

and d) are simulated PSFs of the EDOF meta-optic at object

distances of 3.5 mm and 14.5 mm respectively, e) Correlation plot

of simulated PSF against the PSF at the central focal point for a

cubic and a conventional meta-lens. The correlation clearly shows

the extension of the depth of focus.
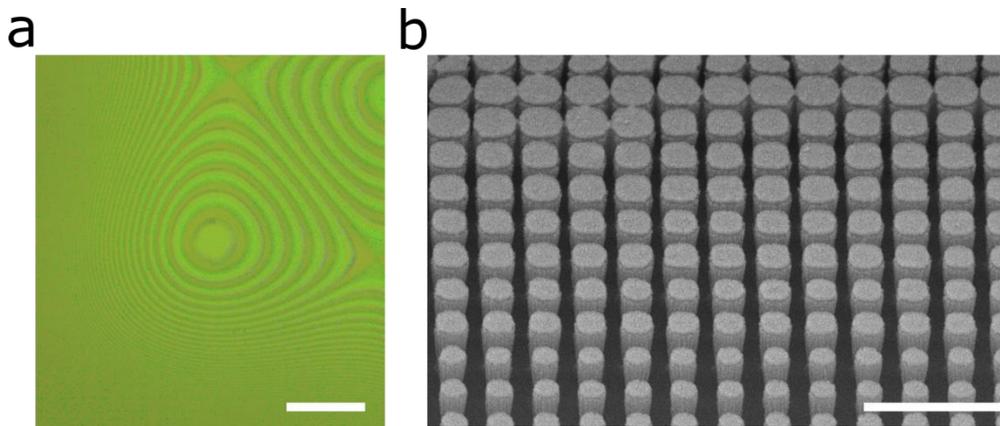
Fig. 4.2. Images of the fabricated meta-optics. The meta-optics was sputter coated

with gold-palladium alloy to ensure charge dissipation a) Optical image (Scale

bar is $150\ \mu m$). b) Scanning electron micrograph; scale bar of $1\ \mu m$ taken at 45°

to the normal.

The meta-optic was then mounted in a 1cm diameter optic holder with standard C-mount threading for characterization. We first measured the PSF of the meta-optic: a $25\mu m$ diameter pinhole is used to approximate a point source, which is illuminated using a green light emitting diode (Thorlabs M530F1). The PSF is captured using a movable microscope (Fig. 4.3a). The position of the pinhole is changed between 7.3mm to 15.1mm from the meta-optics, and the same range is used for the position of the camera (Fig. 4.3b). We can clearly observe that the PSF remains unchanged for various image and object distances. We note that, we are measuring the PSF for a finite conjugate system, as we will use a similar setup for imaging as well. We also confirmed that the minimum focal length for our meta-optic is ~3.5 mm, making the highest NA of the meta-optic 0.28, as predicted by the numerical simulation.
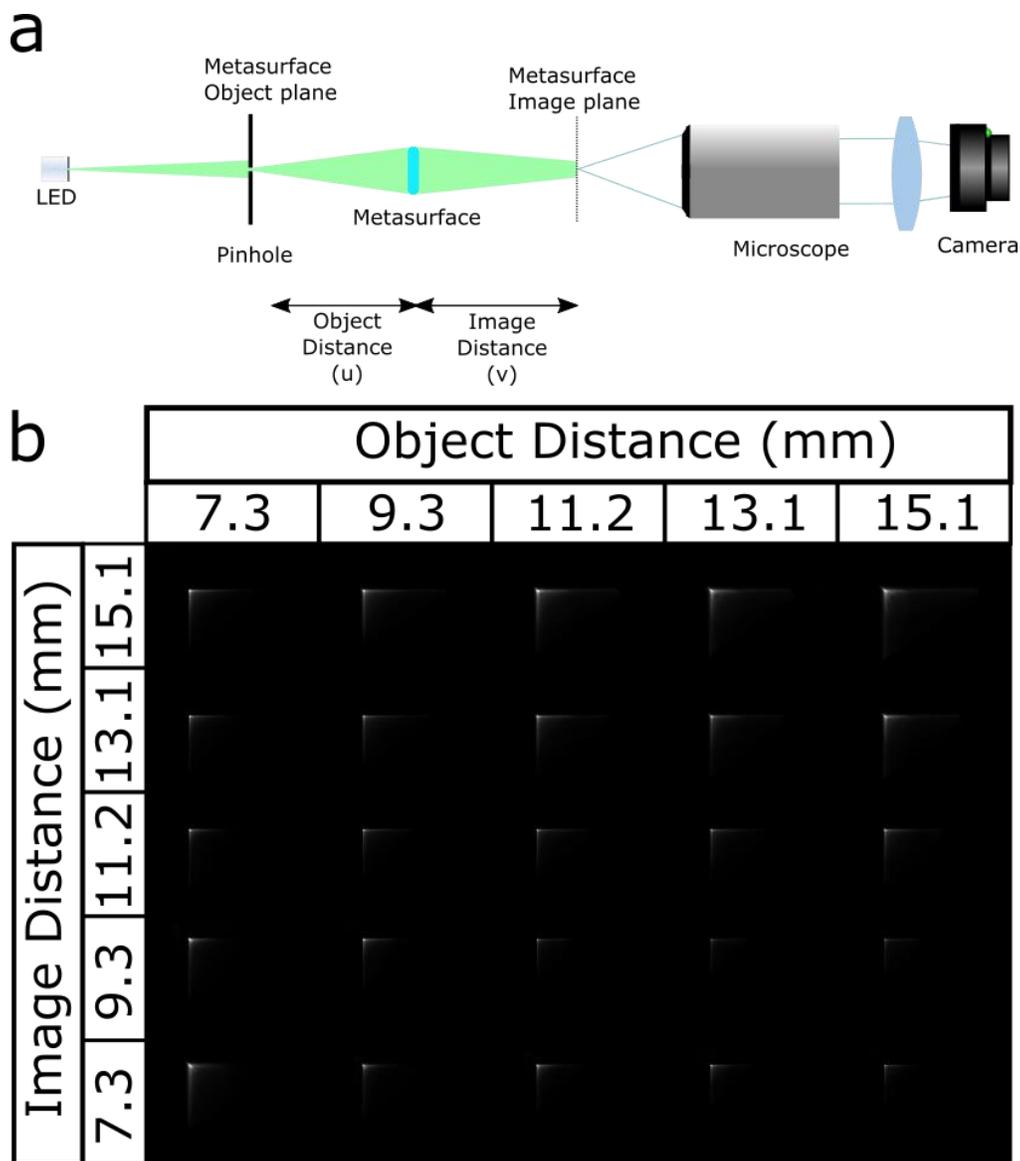
Fig 4.3. a) Setup for PSF measurement. b) Image of 25um pinhole. Image and object plane sweep. Illumination is using a 530nm LED with 33nm bandwidth.

We then tested our system by imaging 1951 USAF Resolution Chart. A metal-coated plate has transparent region showing the Air Force pattern, which is illuminated using the same LED that was used in the PSF measurements. The

images of this backlit pattern were taken at various object (u) and image (v) distances to test the extended depth of focus capability of the lens. From simple ray-optics, we can write for a lens with focal length f

$$\frac{1}{u} + \frac{1}{v} = \frac{1}{f}$$

As a cubic EDOF meta-optic does not produce a lens-like PSF and the raw captured images do not resemble the object, we need to deconvolve the captured sensor data to extract the in-focus image. Several different deconvolution routines, including Wiener, Richardson-Lucy and neural network can be performed to extract the image[42], [43]. Here, we apply a routine based on Total Variation (TV) regularization to deconvolve and denoise the latent image (Fig. 4.4a). This deconvolution method optimizes the sum of the gradient magnitudes while deconvolving the image [44]. As we are performing the imaging under incoherent light, we can model the whole imaging process as a linear system if the camera is not saturated. We ensured that the intensity of the measured PSF did not exceed the maximum threshold of the camera to conserve the linearity of the measured PSF. We also assumed that the PSF was shift-invariant, or that the PSF would remain constant if the pinhole were shifted laterally. This assumption breaks down for large lateral displacements and taking multiple shifted PSFs while using a shift-variant deconvolution technique may produce better results[45]. In our work, this means we have a constrained field of view to ensure the shift-invariant property of our PSF. The imaging shows here show the same range of tunable focal lengths as from the PSF measurements. We note that, such focus tuning however does not require

a varifocal optics, and we term this as digital tuning. We estimate the spatial resolution of our meta-optics via the line-cuts from the measured patterns for object (image) distance of 9.3mm (13.1mm) (Fig. 4.4b). The First column shows the line-cuts from the horizontal lines and the vertical lines are shown in the second column. We can see that for the horizontal lines, we can differentiate lines of thickness of $\sim 8\mu m$, whereas, for vertical lines only $\sim 11\mu m$ lines can be resolved. We attribute this asymmetry to the asymmetric PSF of the cubic EDOF meta-optics. Lines below $\sim 8\mu m$ cannot be resolved by our EDOF lens. We estimate the diffraction limited resolution for a lens under the same condition to be $\sim 1.4\mu m$. The lower spatial resolution comes from the extended PSF of the cubic meta-optics, compared to a lens. However, as explained earlier, the EDOF meta-optics can be used to create images for different object and image distances, which will not be possible with an ordinary metalens.
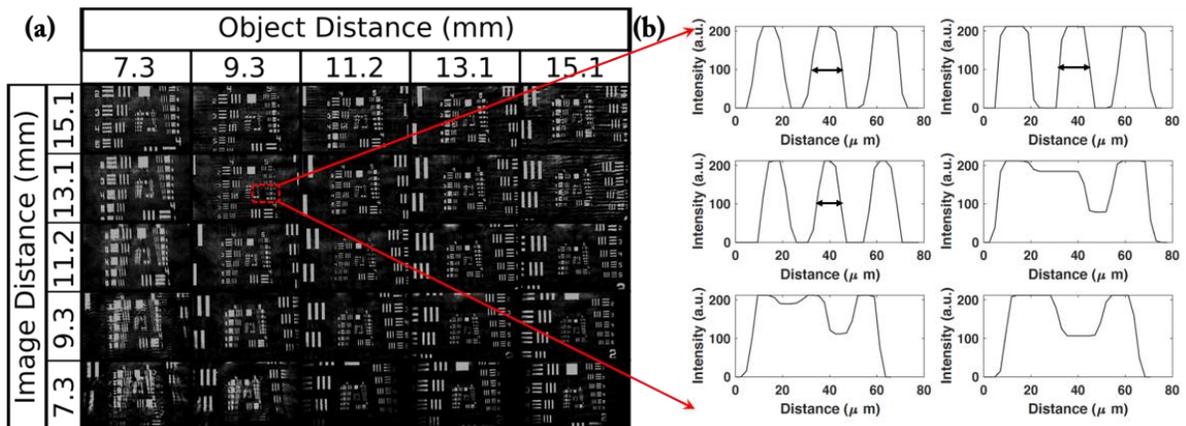
Figure 4.4. (a) Image of the Airforce Resolution chart for different image and object planes. The object distance is the separation between the transparency and the meta-optic while the image distance is the distance between the meta-optic

and the camera. The object is illuminated via a 530nm LED with 33nm bandwidth (full width half maxima). (b) Line cut of the air force chart (for object distance of 9.3mm and image distance of 13.1mm) to estimate resolution: first column is for horizontal lines and second column is for vertical lines.

Thus far in our experiments, we have used a microscope to relay the image produced by the EDOF meta-optic to the sensor for imaging. With a larger aperture meta-optic, it is feasible to image directly onto an off-the-shelf camera module (E-consystems See3CAM_10CUG). For integration, the meta-optic is scribed into a circular piece, and mounted in a C-thread optic mount (Edmund Optics #63-979). The meta-optic is then attached to the camera module using a CS-mount, with a flange back distance of approximately 12 mm, and the final package is shown in Fig. 4.5a. In this configuration, the imaging system has a full field of view of 28° when measured along the sensor diagonal.

We tested the imaging capabilities of the EDOF camera and compared it to an off-the-shelf plano-convex F/2 refractive singlet with focal length 6 mm (Edmund Optics #32-952) by imaging a series of QR codes at different object distances. Both the EDOF meta-optic and refractive singlet lens are tested using the same camera module and with the same CS-mount, ensuring the same sensor characteristics and magnification. The QR-codes are illuminated using a commercially available green LED ring light. The EDOF meta-optic and the refractive singlet have nominal focal lengths that are optimal for imaging at a finite conjugate distance of 13 mm. As seen in the Fig. 4.5b, both imaging systems are fully capable of resolving the QR

code, but the refractive singlet displays improved brightness and contrast when compared to the EDOF meta-optic. As we move the object plane further out, however, the difference between the EDOF meta-optic and refractive singlet widens. For the object distances of 25 mm, 50 mm, and 80 mm, the refractive singlet is incapable of resolving the QR code, while the EDOF meta-optic reliably resolves the barcodes throughout the range of object distances.

When compared to our EDOF meta-optic (F/2.8, focal length 5.6 mm), the refractive singlet has a similar focal length (6 mm vs 5.6 mm), but a larger diameter (3 mm vs 2 mm). The superior brightness and contrast of the singlet at the object distance of 13 mm is attributed both to the larger diameter of the refractive singlet, and also the properties of the EDOF meta-optic itself. At an aperture of 3 mm, the refractive optic has a surface that has twice the area of the EDOF meta-optic and is able to more than double the light collection. In addition, the EDOF meta-optic operates by sacrificing some contrast at the nominal object distance in favor of extending the depth-of-field significantly.
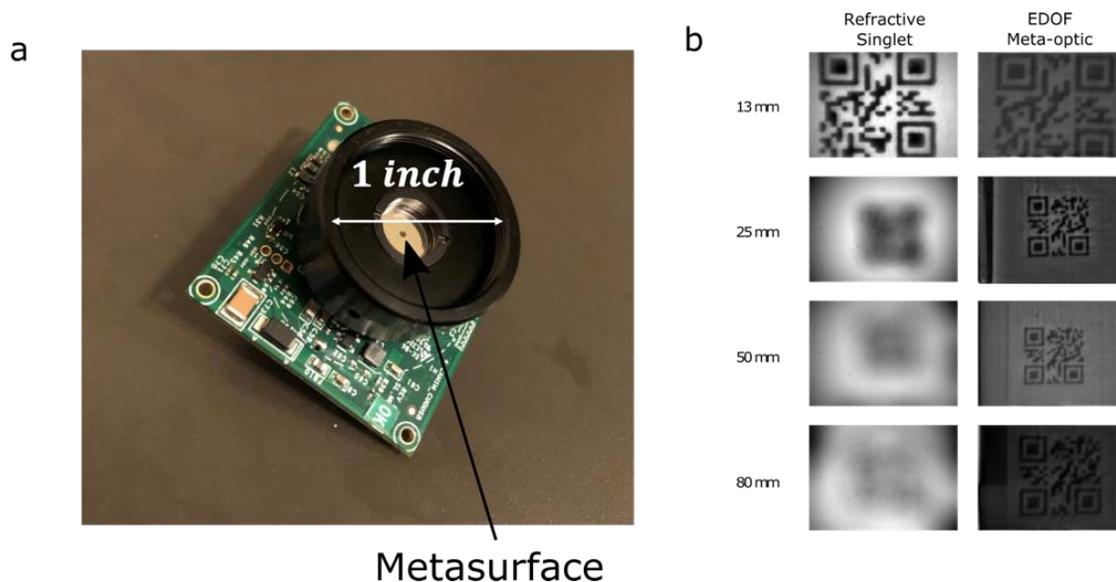
Fig. 4.5. a) Metasurface optic integrated with E-consystems camera module. b) Pictures of QR code object at differing object lengths taken by a singlet refractive lens with focal length 6mm at F/2 (left) and by a singlet EDOF meta-optic with nominal focal length 5.6mm at F/2.8 (right). The 13mm and 25mm object distances used a $5mm \times 5mm$ QR code. The 50mm object distance used a $10mm \times 10mm$ QR code, and the 80mm object distance used a $30mm \times 30mm$ barcode.

We reported an EDOF, $f/1.75$ cubic meta-optics with highest NA of 0.28, thanks to the subwavelength periodicity of meta-optics. The EDOF nature of the meta-optic was probed using PSF measurements and imaging experiments. We also reported the development of an EDOF meta-optic camera module using a commercial sensor and demonstrated QR code imaging at different object distances. Our work opens opportunities for system-level integration of meta-optics with commercial sensors, and the simplification of the tunable imaging systems exploiting EDOF properties. This new class of EDOF imaging systems could find applications in industrial production lines[46], compact image sensors, biological imaging[47], [48], and automobile navigation and driver monitoring systems. Going beyond EDOF, such "software defined optics" could potentially transfer many of the hardware functionalities to software and accelerate the co-design and co-integration of hardware and software for free-space optics.
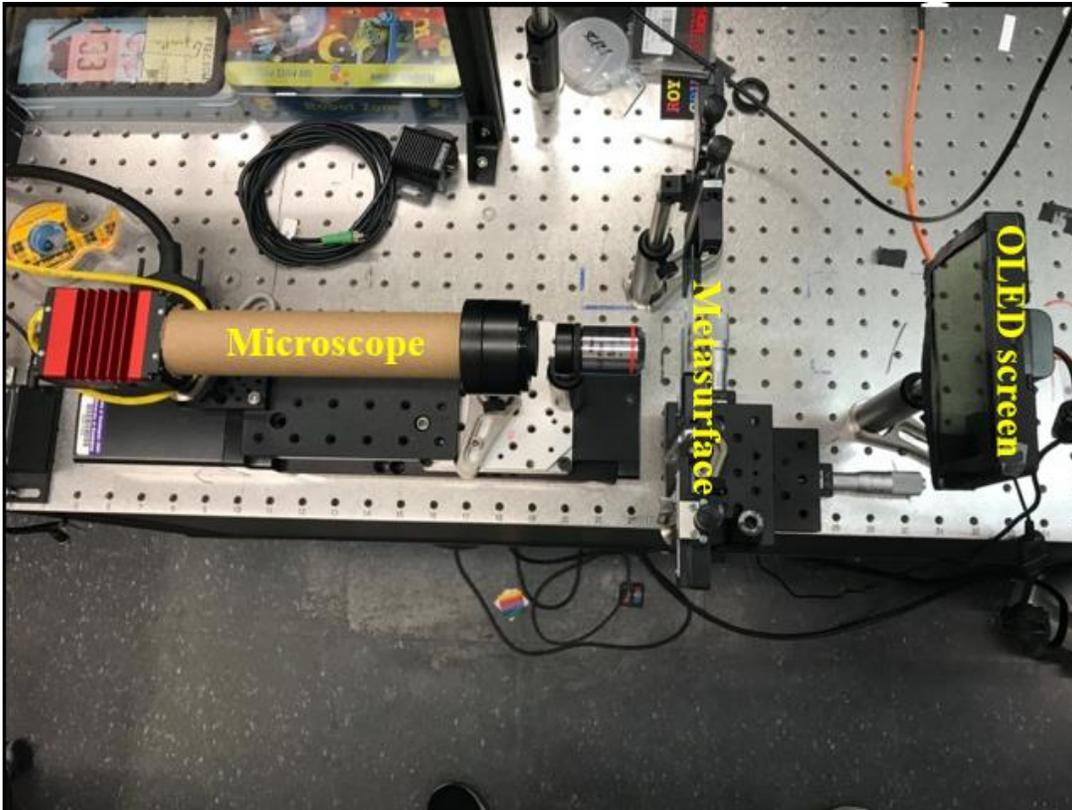
Figure 4.6 Metasurface measurement setup.

Figure 4.6 shows the setup used for the metasurface measurement. On the left is a microscope that can translate along the optical axis. The metasurface device under test sits on an x, y, z translatable stage. Finally, a light source is placed in front of the metasurface. In this case, an LED display is in place since it can produce very high contrast and narrow bandwidth red, green, and blue images.

The translatable microscope is useful since it allows for collection of light from planes extremely close to the substrate and can automatically scan the 3D intensity distribution. The ability to collect light near the substrate is important since many of optics have focal lengths near to the substrate thickness and moving an exposed CCD that close to the device would be difficult.

5. Inverse Design

In many cases, there is no clear way to represent the optimal design. Previously, a design for a meta-optic was created and the performance was evaluated. In some cases, it can sometimes be advantageous to instead start with a desired function, and then determine the design that would be able to represent. This is at the core of inverse design. This section will discuss the methods of using auto-gradient methods to optimize phase masks and neural networks for scatterer optimization.

5.1. Inverse of Phase Masks using auto-gradient methods

The angular spectrum method mentioned before, or various other propagation methods can be used to model the propagation of waves through space. A key aspect of this method is that all operations are differentiable with respect to the phase mask phases. Therefore, for a given phase profile with a known incident field, an instantaneous derivative can be taken for the propagated light with respect to the phase profile. This allows for iterative gradient-based optimization methods to be used to adjust the phases so that the output field is close to its desired value.

$$U_1(x, y) = propogation(\phi(x, y), U_0(x, y))$$

The field at the destination plane is a function of the incident field and the phase profile of the phase mask. For example, if the intensity of the field at x=0, y=0 should be maximized, the merit function $F = |U_1(x = 0, y = 0)|^2$ would be maximized.

By taking the derivative of the merit function with respect to the total phase profile, the phase profile can be iteratively updated using the following method

$$\phi_i = \phi_{i-1} + \gamma \nabla F(\phi_i)$$

Where ϕ_i is the phase profile for the ith iteration, and γ is a positive scalar called the learning rate. The leaning rate can be adjusted to change the stability and speed of the optimization.

Manual differentiation of these forward functions and associated merit functions can be cumbersome and error-prone so an auto-differentiation software library can be used with little performance disadvantage over using manually calculated derivatives. There are several auto-differentiation libraries available including Google's Tensorflow [49]and Meta's Pytorch[50] . Since these popular artificial neural network libraries predominantly use auto-differentiation to train and have efficient implementations, they provide a good resource for general purpose auto-differentiation. Also, they support fast linear algebra algorithms that use various application specific hardware accelerators such as graphical processing units and tensor processing units.

It is helpful to visualize equations as directed, acyclic graph. Nodes can either represent constants, variables, or operations between nodes. Only operators can have child nodes as the operators act and their children. The auto-differentiation process can take this graph and calculate instantaneous derivatives recursively by applying the chain rule on the children.

Since this process only calculates the instantaneous derivative (the derivative that is evaluated that the current value of the parameters), this process must be computed repeatedly after the parameters are adjusted. Propagating the derivative from the

merit function to the parameters, which we use here, is called reverse mode auto-differentiation.

This method makes changes to the merit function easy since the graph is generated automatically from the code, instead of having to manually calculate derivatives which in not time efficient when rapidly modifying the structure of the optical system.

The phase mask is represented as a discrete, rectangular grid of phases. The discretized phase is applied to the complex, discretized field. When optimizing both magnitude and phase of the mask, special attention must be taken such that the magnitude of mask is bounded by between 0 and 1, or so that there is no gain in the system. One solution to this problem is to define the magnitude in terms of a free parameter that has arbitrary range, but smoothly thresholds the parameter so that gradients can transfer. One example of such a function is a hyperbolic tangent

$$|\boldsymbol{U}| = \frac{tanh\left(\frac{\boldsymbol{t}}{a}\right) + 1}{2}$$

Where U is the field grid, t is the grid of free parameters, a is a scaling factor. Since floating-point systems have finite precision, gradients that are too small can be lost in underflow, so the slope of the hyperbolic tangent function can be adjusted to change the range where this occurs.

The function does not have to map one-to-one either. Periodic functions such as cosine can also be used to constrain the free parameter. More complex methods can be used to ensure learning rate for the free parameter is low enough to bound the

parameter to within a period of the cosine function so avoid hopping. Phase optimization has no such issue (other than issue represented in floating point overflow) since any phase that is offset by an integer multiple of 2π is equivalent when dealing with time harmonics.

In most cases, the phase-transmission function of a given set of scatterer geometries is known as the in figure below.
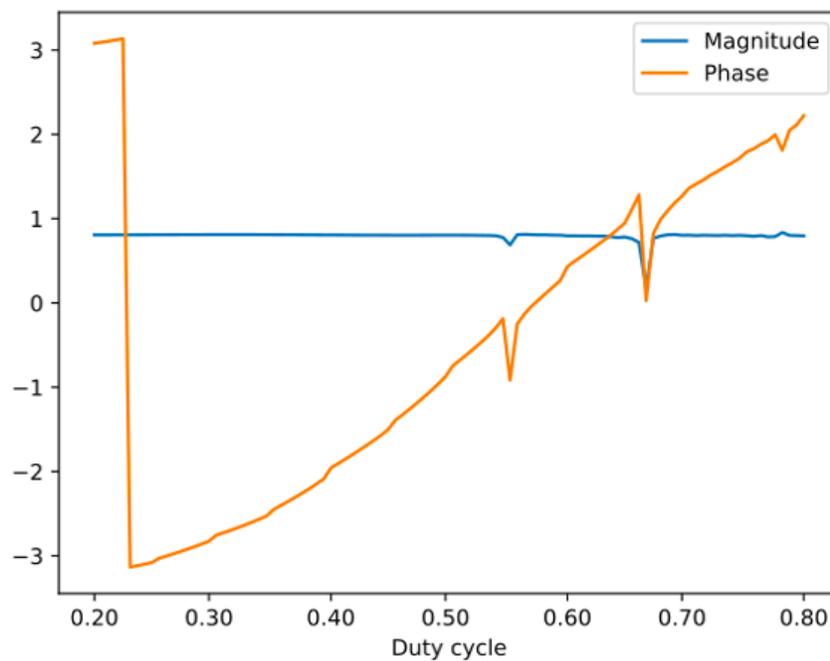
Fig. 5.1 – Example of a phase and intensity plot vs duty cycle for a scatterer.

Excerpt from [22]

This data can be used to pin the phase with an associated transmission. To increase the accuracy of the optimization, a free parameter can be used to drive the physical properties of the scatterer followed by a threshold function. The scatter geometry can then be differentiably mapped to actual transmission of the scatter using a fit to

simulation data. This way, the free parameter will be optimized while representing the geometry, phase, and magnitude in the simulation.

$$|T| = F(Geometry(t))$$

$$\angle T = G(Geometry(t))$$

Where F maps some aspect of geometry to the transmission magnitude and G maps that aspect to the transmission phase. The geometry function is a threshold function that takes the free parameter and differentially maps it to values that are in an acceptable range for the design.

5.2. Inverse Design of Scatterers

Conventional simulation of transmission characteristics for meta-atoms includes using a rigorous electro-magnetic simulation method to determine the transmission characteristics of each element. However, certain simplifications must be made to keep simulation time reasonable. Once assumption is that the geometry of neighboring scatters has little to no effect on the transmission characterizes of the pillar. This is called the local phase approximation. This restricts the efficiency of quickly varying geometries such as at Fresnel boundaries or at large phase gradients. To address nearest neighbor effects, a model that can determine the transmission of a pillar as a function of the pillar geometry and its nearest neighbors. Values for this function can be determined using rigorous electro-magnetic simulation but a continuous, differentiable function is difficult to analytically define since this problem is non-linear and complex.
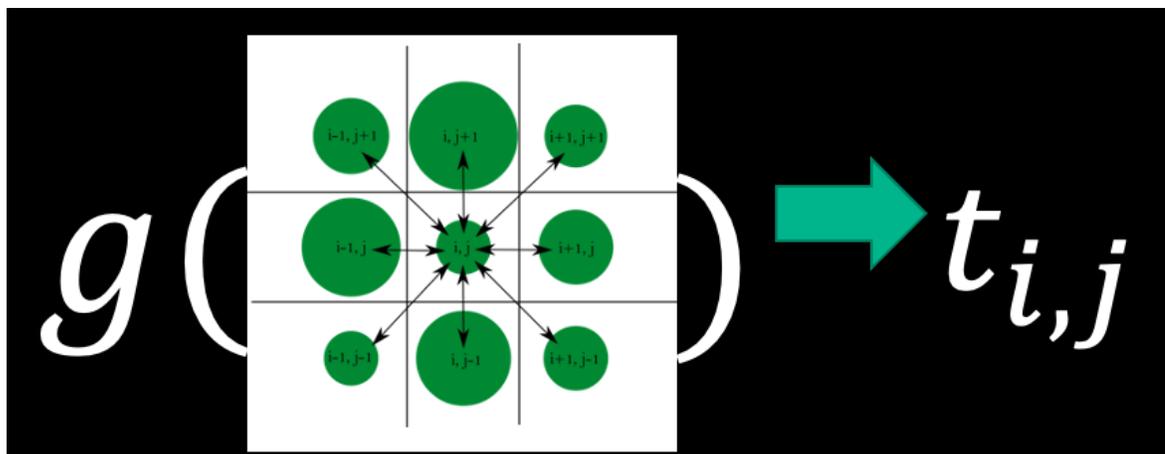
Figure 5.2 - Diagram representing transmission coefficient over the central

scatter as a function of geometry of central scatterer and nearest neighbors.

This is a highly non-linear problem where small changes in neighboring scatterer geometry will have large effect on transmission phase and magnitude. The functions that are inherent to the physics are difficult to determine so some derived function that can perform this mapping could be used. It is relatively easy to generate large amounts of data that covers the desired input space. Calculating this structure using FDTD is only several microns deep (at visible wavelengths) and it is most efficient to simulate 30×30 grids of random scatterers. The near field over overlapping 3×3 set of scatterers is then sampled. Only scatterers that are far from the simulation boundaries are selected. This can generate tens of thousands of data points per a day.

Non-linear mapping between one high dimensional space to another high dimensional space can be easily performed using artificial neural networks.

Artificial neural networks are a series of matrix multiplications, vector additions, and non-linear functions in arranged in various topologies. An input vector can be

operated on by these operations and an output vector is produced. If a set of input and output vectors are known, gradients of the error between the expected output and actual output can be taken with respect to the matrix and vector values. Using gradient descent, the matrix values (weights) and vector values (biases) can be adjusted until the error is minimized.

This is essentially fitting a non-linear, high dimensional function that maps one space to another and is useful when the underlying function is unknown. The weights and biases define the function and can represent various known complex functions given sufficient network complexity and training.

Since this problem is non-linear, linear statistical methods may not work as well. Also, the structure of the function is hard to determine so various direct non-linear methods will also not work. The neural network will learn the non-linear function through training and the addition training data and computation complexity over an analytic method is manageable in this case.

6. Spatial Light Modulator Cavity Design

While metasurface on their own have increased the design flexibility of optics in many areas, there are a variety of fields that would benefit when combined with tunability. Notably, spatial phase modulations can be applied to LIDAR which is receiving strong attention in autonomous navigation and augmented reality.

Also, they can be used for imaging though disordered media such as tissue and blood where the effect of the scattering can be inverted using a dynamic phase mask. Metasurfaces can be cascaded to perform mathematical operations on 2D wavefronts allowing for massively parallelized linear computations. A historical example of this is with conventional optics where 2D Fourier transforms are performed on images, but metasurfaces allow for more general operations such as image classification. Finally, tunable metasurfaces can be generally applied to beam steering.

Current Spatial Light Modulators (SLMs) enable a wide variety of programmable optical wavefront manipulations. These include adaptive optics, optical vector-matrix multiplication, optical neural networks[27], and focus tuning. However, for such applications, current SLM speed is limiting. MEMS offer high speed but are expensive to manufacture, are more sensitive to the environment, and require high voltage power supplies while liquid crystals are fundamentally limited in their polarization speed. A robust high speed SLM is necessary to advance these fields Here we propose an alternative method, based on an Electro-Optic (EO) polymer, that is both high speed and robust. By placing EO polymer within a metal-metasurface cavity, large phase shifts are achieved at relatively low voltages. Devices based on this polymer have achieved modulation speeds of 10GHz[51].

6.1. Pockels Effect

A material that exhibits a change in refractive index when an electric field is applied to is called an electro-optic material.
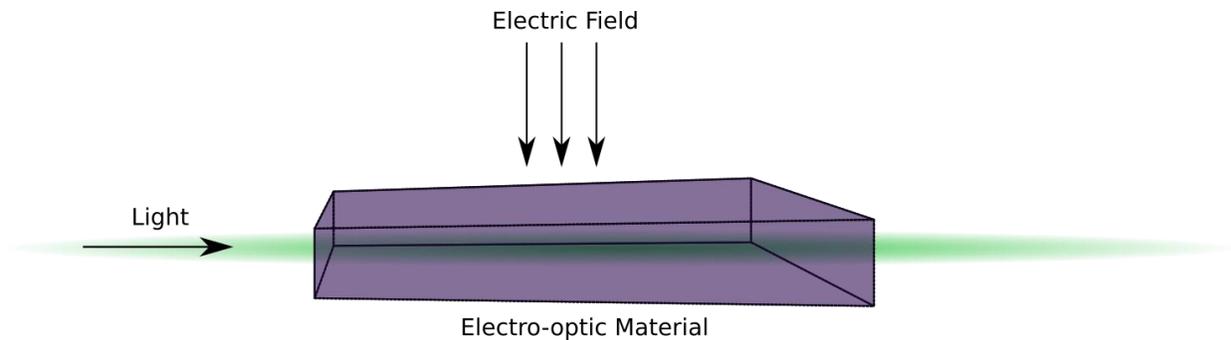
Figure 6.1 - Light traveling through an electro-optic material.

The effect of the electric field on the refractive index can be described as a Taylor expansion around E=0.

$$n(E) = n + a_1 E + \frac{1}{2} a_2 E^2 + \cdots$$

When the relationship between the field applied and refractive index is linear, that material is called a Pockels material, and a_1 being the Pockels coefficient.
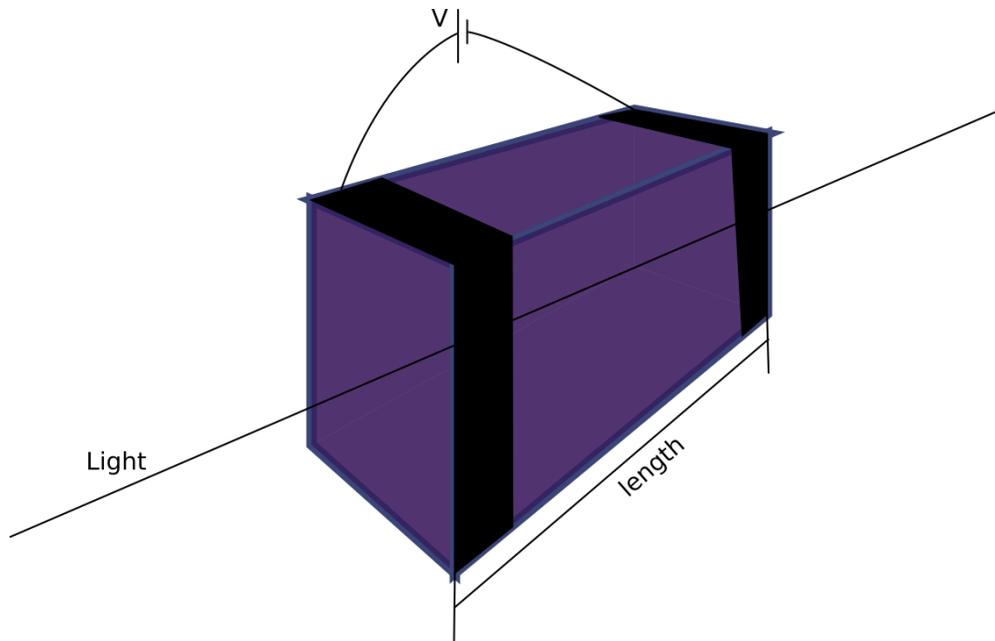
Figure 6.2 - Longitudinal electro-optic modulators.

A first order approximation of our EO polymer system is shown in figure 6.2 where the electric field is applied along the optical axis and transverse to the polarization.

When the polymer is polled during fabrication, the molecules align, and the polymer acquires some long-range order. This system can be approximated as a uniaxial crystal where the optical axis is parallel to the direction of propagation.

The index ellipsoid of a uniaxial material, where the extraordinary crystal axis is parallel to the external electric field. In bulk material, this indicates that the apparent refractive index for light traveling in the z direction is independent of polarization.

6.2. Electrode design / Metasurface reflector

To make an electro-optic tunable cavity, it is not only necessary for both ends of the cavity to be reflective, but they must also be conductive. For the back electrode, it is simple to add a continuous metal films. Metals are conductive at can be reflective at optical frequencies. However, to have spatially varying phase change across the device, at least one side of the cavity should support a spatially varying potential. This can be done by splitting one electrode into a grating. However. when done blindly, this will reduce the reflection of the electrode and lead to a smaller phase shift per voltage. The solution to this problem is to design the addressing electrode such that it reflects strongly which can be done using electromagnetic simulation

Electromagnetic Waves Frequency Domain (EWFD) and Electrostatics (ES) modules of COMSOL Multiphysics Finite Element (FE) simulation software was primarily for design simulation. Lumerical Finite Difference Time Domain (FDTD) was used for verification of the FE model since it uses a significantly different method of simulation albeit slower for single frequency and narrowband simulations. Due to a limitation with the FDTD software implementation, we cannot use a spatial varying and dispersive material. To model the system accurately, this is required. Therefore, only a uniform electric field was used in verification.

Relevant materials were deposited and measured using ellipsometry for final design of the pixel. See figures 6.3 and 6.4.
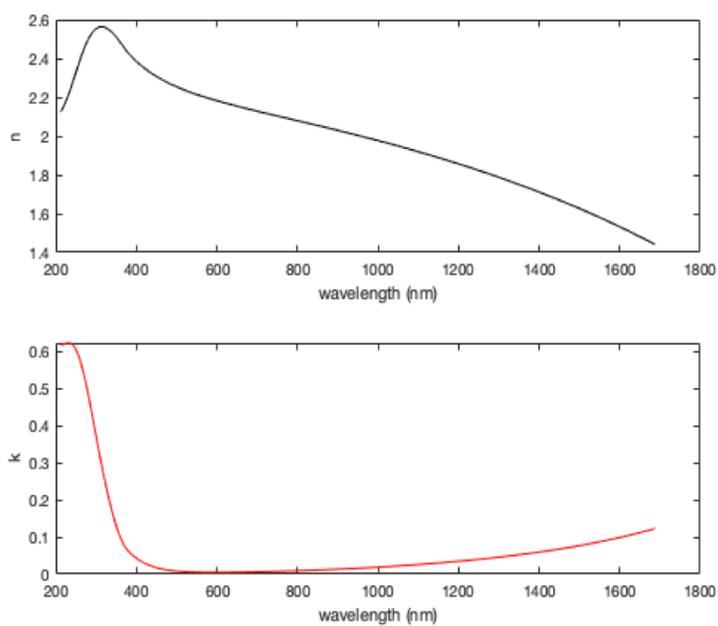
Figure 6.3. Averaged ITO refractive index. Real (top) and imaginary (bottom) versus

wavelength. Measured using ellipsometry
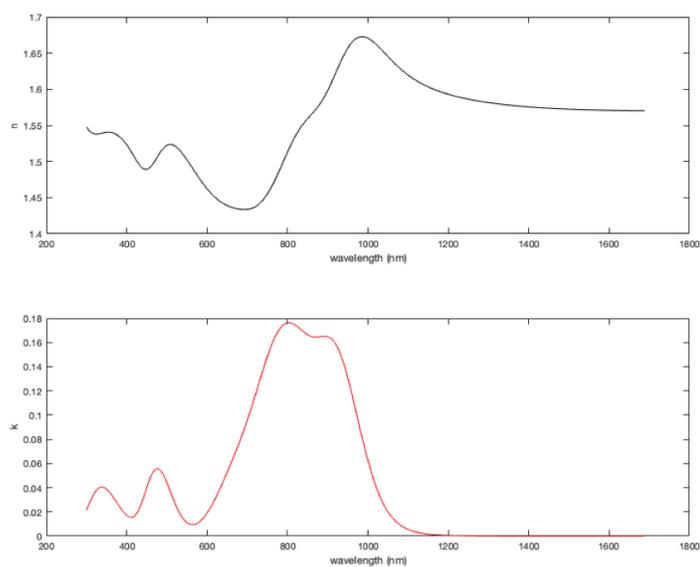
Figure 6.4 EO polymer refractive index. Real (top) and imaginary (bottom) versus wavelength.

Measured using ellipsometry

The design process entailed finding a conductive grating geometry that has high reflectivity with a geometry shown in figure 6.5. This grating was then used as a mirror in the cavity and an optimal cavity length was defined. Properties including periodicity, height, and width are swept such that the reflectivity was maximized. Table 6.1 shows the optimized parameters and Figure 6.6 showns the corresponding reflection spectrum.

Table 6.1 - Final geometry of the grating

Parameter	Value
Wavelength	1550nm
a-Si thickness	245nm
period (a)	1.2um
cavity length	1um
dc	0.62
r13	100pm/V
r33	300pm/V
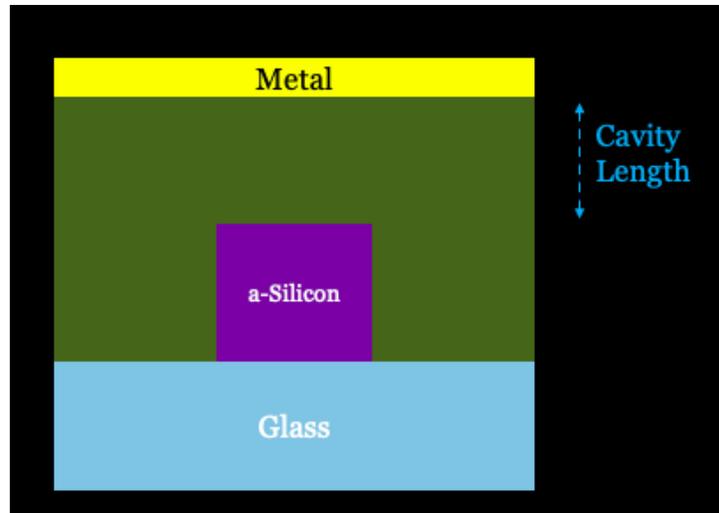
Figure 6.5 – Geometry cross section of a single grating
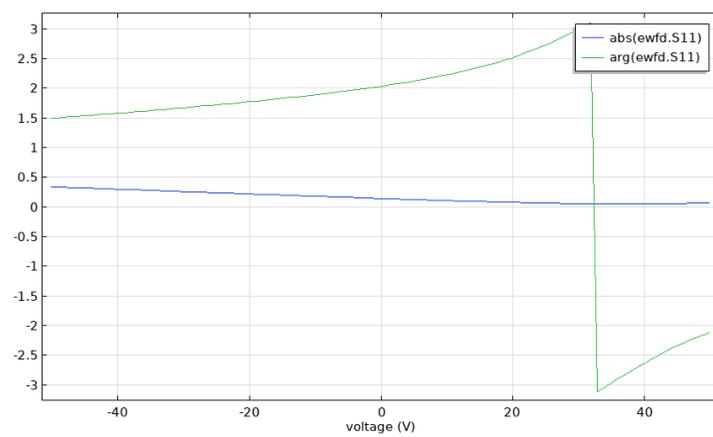
Figure 6.6 - Reflection spectrum from the grating versus applied voltage. Note the π phase shift

over the 100V span.

6.3. Methods

While a design may work in simulation, it must also be fabricable. Here is the fabrication process flow for the previously designed structure.
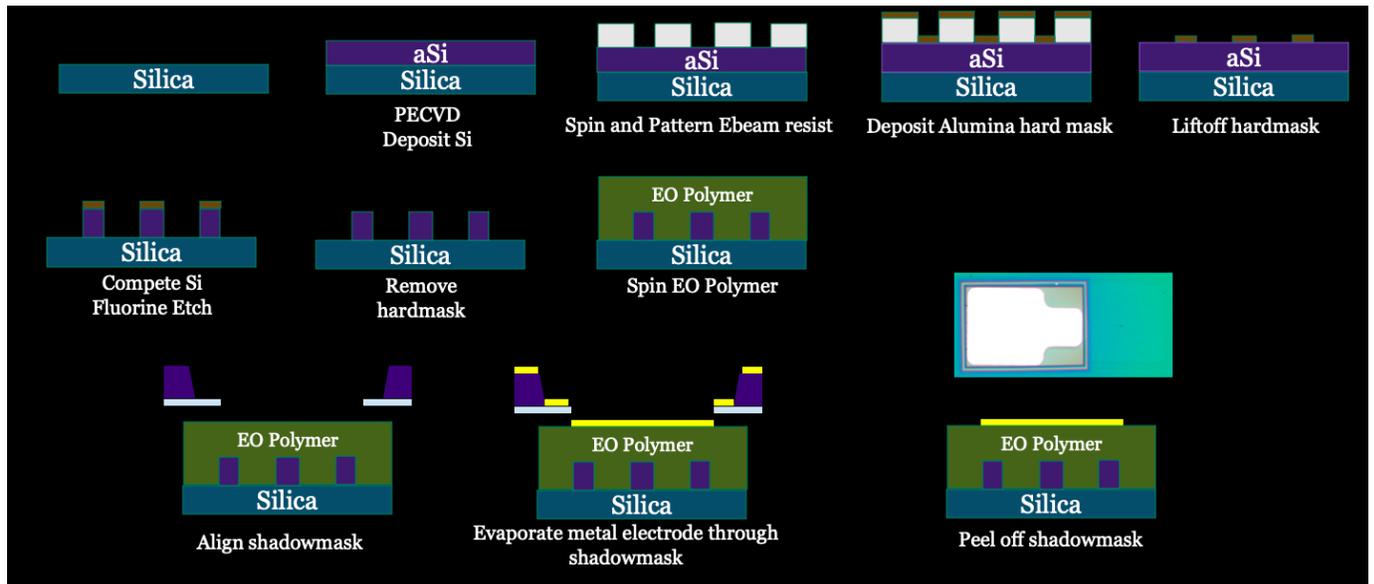
Figure 6.7 – Grating fabrication process flow

Starting with a glass wafer, amorphous silicon is deposited in a plasma enhanced chemical vapor deposition chamber. Electron beam resist is spun on the surface of the wafer and the grating pattern is exposed in the electron beam lithography tool. The exposed patterns are developed away and an aluminum oxide hardmask layer is evaporated onto the device. The hardmask is lifted off and the silicon is etched in an inductively coupled plasma etcher with fluorine chemistries. The hard mask is then removed. A layer of the electro-optic polymer is deposited using a spin-coater.

Defining the top electrode was quite difficult since the electrode must be patterned but most chemicals require for lithography were found to react with the polymer film. Various potential solutions were tried such as atomic layer deposition and chemical vapor deposition to isolate the

developer and photo-resist solvents from the polymer. However, they suffered from pin-holing and cracking after heating leaving gaps for the solvent to penetrate. The final solution we found was to fabricate a floating silicon nitride membrane which we were able to use as a shadow mask. The metal would pass in regions where the membrane was etched but prevented from depositing by the rest of the floating membrane.
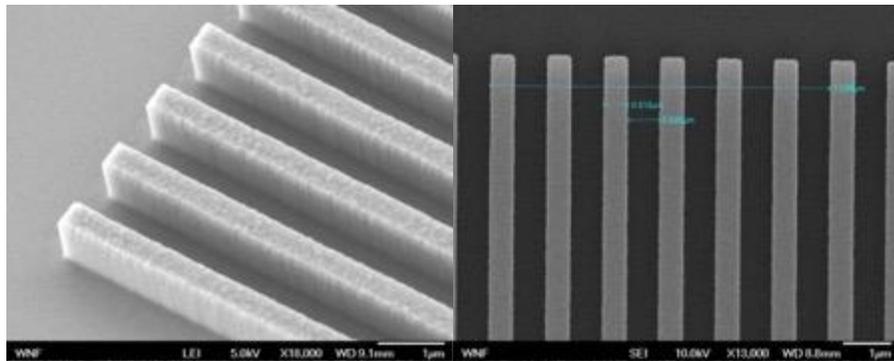
Figure 6.8 - Si deposited on substrate post etch.

The EO polymer is spun on the grating and dried in a vacuum oven. Another shadow mask is aligned and 100nm of gold is evaporated to form the back electrode.
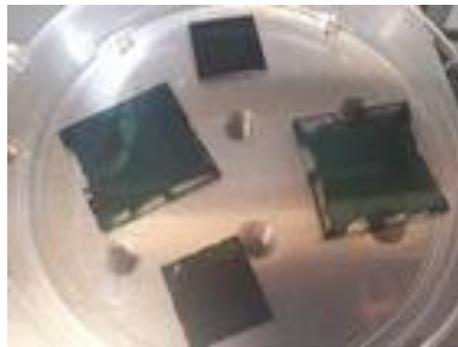
Figure 6.9 - Spin-coated EO polymer

Figure 6.10 shows the single pixel layout with the metal pad and grating attached to a common pad. Probe needles will contact each pad to bias the material between the two electrodes.
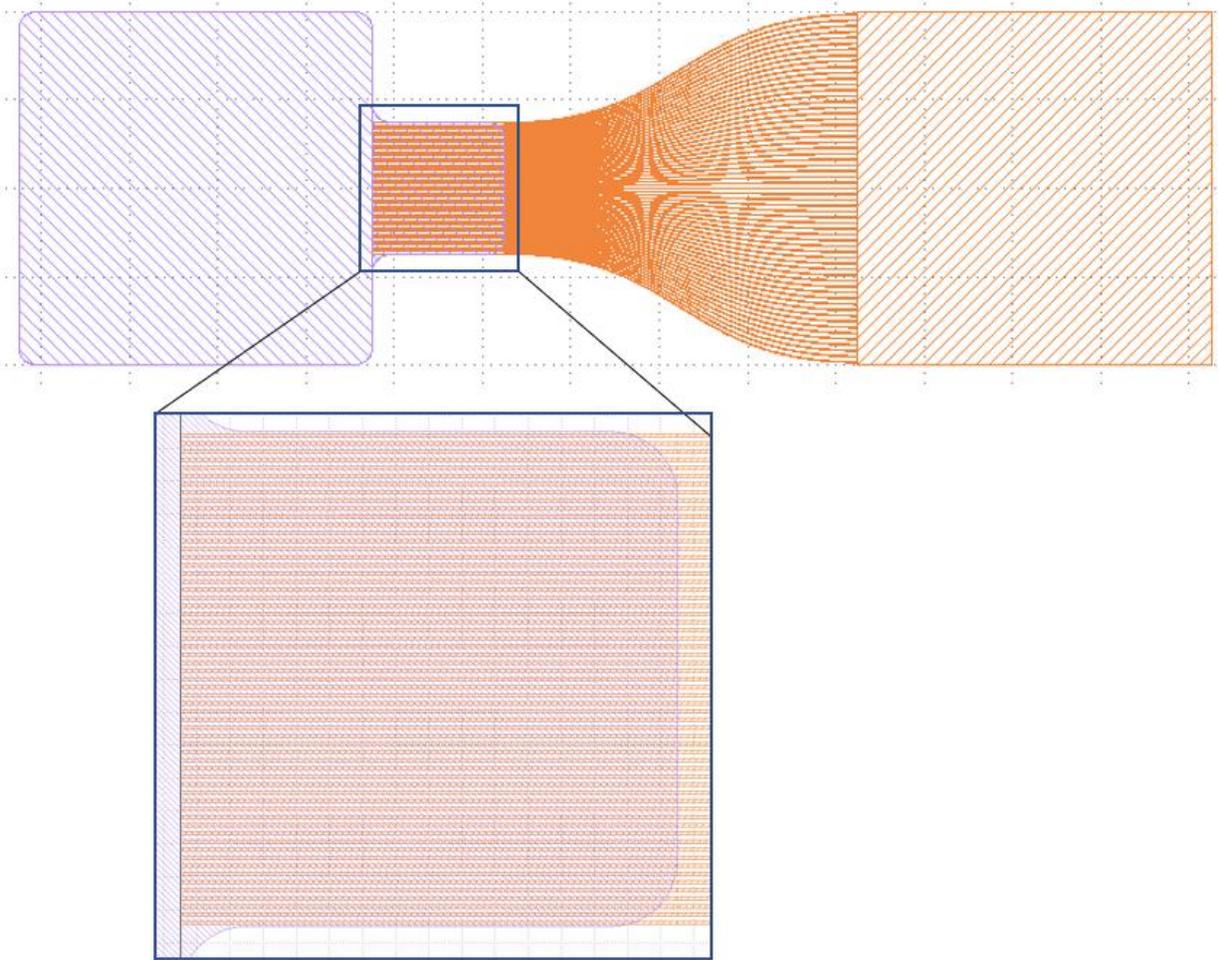
Figure 6.10 – Design of single pixel cavity

6.4. Further iterations

To have electrically addressable pixels, control lines need to be added. This will be implemented in future tests. Metal fanout pads will be wire bonded to a PCB and will be controlled by several high voltage multi-channel DACs.

7. 1D-to-2D SLM

This section is adapted, with permission, from *2D beam shaping via 1D spatial light modulation*
James E. M. Whitehead, Albert Ryou, Shane Colburn, Maksym Zhelyeznyakov, Arka Majumdar.

Many emerging, high-speed, reconfigurable optical systems are limited by routing complexity when producing dynamic, two-dimensional (2D) electric fields. We propose a gradient-based inverse designed, static phase-mask doublet to generate arbitrary 2D intensity wavefronts using a one-dimensional (1D) intensity Spatial Light Modulator (SLM). We numerically simulate the capability of mapping each point in a 49 element 1D array to a distinct 7×7 2D spatial distribution. Our proposed method will significantly relax the routing complexity of electrical control signals, possibly enabling high-speed, sub-wavelength 2D SLMs leveraging new materials and pixel architectures.
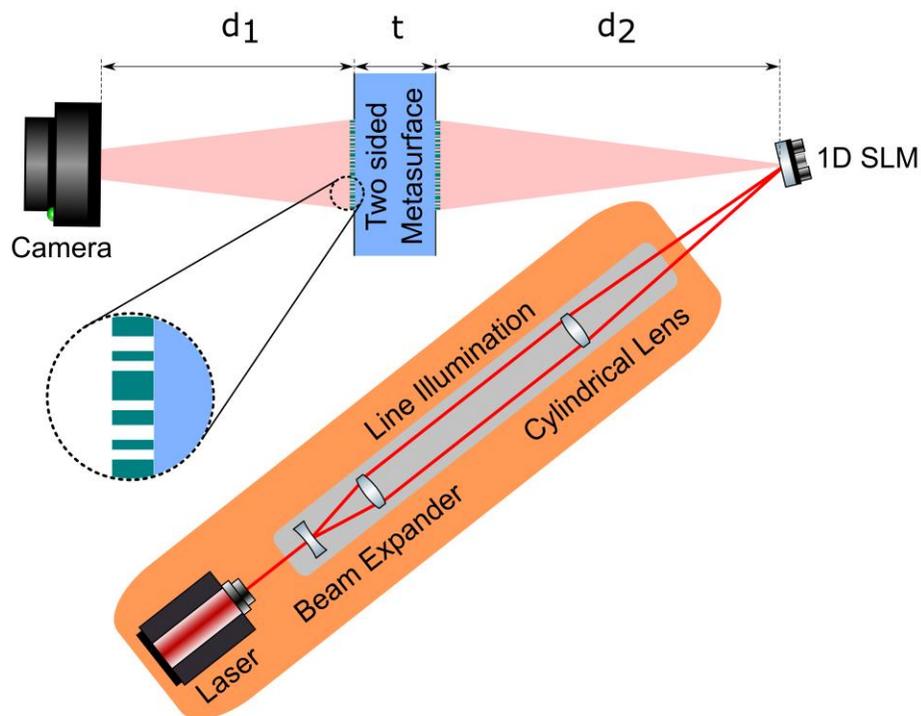
Figure 7.1. Proposed optical architecture for using 1D SLM for 2D wavefront shaping. Coherent light is focused into a line to efficiently illuminate a linear array of pixels (1D SLM). The modulated light is sent to a pair of meta-optical structures. After passing through the meta-optics doublet, the light is captured in a camera, where the arbitrary 2D patterns are observed. The gap between the 1D SLM and the first phase mask is kept at $d_2 = 2\ mm$. The separation between two masks is $t = 1\ mm$, corresponding to a standard glass wafer thickness so that masks can be fabricated on either sides of a substrate [52]. The distance between the final mask and the camera is $d_1 = 2cm$.

Fast, dynamic manipulation of two-dimensional (2D) optical fields is integral to many emerging applications including optical holography [53], non-line-of-sight imaging [54], optical neural networks [27], [55] and imaging through disorder [56]. Currently, most of these applications rely on either digital micromirror devices (DMDs) or liquid crystal-based spatial light modulators (SLMs). Both technologies suffer from low-speed operation (~1-100 kHz), due to large inertia and high-power consumption of the liquid crystals or mechanical mirrors. Many of the aforementioned applications will, however, require much higher speed (~100MHz-1GHz) modulation.

Field-induced electro-optic modulation via free carrier dispersion [57] or the Pockels effect [58], can potentially increase the speed by several orders of magnitude, as evidenced by their use in high-speed optical interconnects. An increase in operating speed, however, must be accompanied by a reduction in switching energy per pixel (E_{sw}) to maintain an acceptable level of power consumption.

For an SLM with N number of pixels operating at a frequency of f_o, the total operating power becomes $\sim E_{sw} N f_o$. For a field-induced modulation method, the switching energy is directly

proportional to the active pixel volume V_m. Maintaining this switching energy at an acceptable level requires $V_m < \lambda^3$, λ being the operating wavelength and is largely independent of the reconfiguration mechanism being used [59]. Such sub-wavelength volume also necessitates the pixel separation to be sub-wavelength. Unfortunately, accommodating a high pixel count 2D SLM with sub-wavelength pitch poses a significant challenge in terms of routing of electrical control wires. A 2D SLM with $N \times N$ pixels will need N^2 control signals with an electrode spacing of $\sim \lambda/N$ to address all pixels along each row. At visible wavelengths where each phase shifter has its own pair of electrical contacts, the most sophisticated semiconductor fabrication techniques cannot exceed N ~10. While using vias (out-of-plane wires connecting conductors in different layers in semiconductor fabrication), we can exploit multi-layers of metallic interconnects, a prohibitively large number of vias will be needed to scale the number of pixels to the state-of-the-art values ($\sim 10^5 - 10^6$). The number of control signals can be reduced to $O(N)$ by exploiting active electronics, including a thin film transistor-based active matrix. While such active electronics are a norm in displays (speed of ~100 frames per second), realizing high-speed operation (~100 MHz, i.e., $\sim 10^8$ frames per second) using active matrix is very difficult even for a modest number of pixels [60]. $O(N)$ signals to control N^2 pixels can also be realized if the changed state of the pixels can be held without an external signal for a sufficiently long time to be periodically refreshed. Unfortunately, most field-induced electro-optic effects are volatile and disappear very soon after the control is removed.

A 1D-SLM, however, is far simpler to address and the routing of the electrical control lines becomes trivial. In fact, there are already several recent demonstrations of 1D-SLMs exploiting free-carrier dispersion effects [57], [61]. We note that, while 1D SLMs are not inherently faster, the ease of routing and architectural simplicity can enable faster modulation effects to be used.

Unfortunately, 1D beam shaping is far less versatile than 2D wavefront modulation. An attractive solution will be to map a 1D array of N^2 phase-shifters to a 2D array of $N \times N$ pixels, which will enable 2D wave-front modulation bypassing the difficulty in routing the electrical control signals. To support this, a recent work [62] used a random medium to enable a 1D-to-2D mapping for imaging: a high speed (~350kHz) 1D mechanically-actuated SLM is used to focus light in a 2D plane through a random medium. However, arbitrary wavefront shaping in two dimensions was not demonstrated.

We propose a method to control a 2D wavefront by modulating the pixels physically arranged in a 1D array. The key is an inverse-designed phase mask doublet, that maps an input point source to a two-dimensional spatial field profile that forms an orthogonal 2D intensity basis. Thus, an effective 2D SLM can be realized using a 1D SLM. Figure 7.1 shows the proposed optical architecture for the 1D-to-2D mapped SLM. The laser light is modulated using a 1D array of tunable pixels, which then passes through the composite phase masks. We design these two phase-masks to route the light from each 1D pixel to produce a desired 2D intensity distribution at a specific plane (here the plane of the camera).

We first construct a forward model that simulates the light propagation from a 1D SLM through the free space and include the light's interaction with discretized phase masks. The phase masks span an area of $2mm \times 2mm$ with 400×400 equally spaced elements. This leads to an element spacing of $5\mu m$. We employ the band-limited angular spectrum method to simulate the forward propagation [31], as shown below:

$$E(x, y, z_0) = E(x, y, 0) * h(x, y, z_o)$$

$$\mathcal{F}\{h(x, y, z_o)\} = e^{j\frac{2\pi}{\lambda}z_0\sqrt{1-(\lambda f_x)^2-(\lambda f_y)^2}} \times A(f_x, f_y)$$

$E(x, y, z)$ is the electric phasor field, $h(x, y, z)$ is the point spread function, $\mathcal{F}$ is the 2D spatial Fourier transform operator, λ is the wavelength of light and z_0 is the propagation distance. The input source field is $E(x, y, 0)$. $A(f_x, f_y)$ is a mask that limits the spatial bandwidth to be lower than f_x and f_y, which blocks high-angle wavevector components that would otherwise wrap around and re-enter the simulation domain [31]. The effect of the phase-mask is modeled by a point-by-point multiplication of the input field with the phase mask's complex amplitudes.

This forward model is then used in an automatic differentiation-based optimization method to design the phase profiles which will map the 1D pixel array to the 2D wavefront. For the optimization, we construct a cost function C based on the desired input-output mapping:

$$C = -\prod_k^N \left(\sum_{i,j} y_k^{(i,j)} \hat{y}_k^{(i,j)} \right)$$

where $y_k^{(i,j)}$ and $\hat{y}_k^{(i,j)}$ are the target and the output spatial distributions respectively for the kth input mode (in this case each pixel in the 1D array). N is the number of pixels in the 1D array. The two-dimensional field is discretized in the (x, y) plane with i and j being the discretization indices. This cost function is designed to make the output modes similar to the desired modes while ensuring that each output mode contains similar power.

The equation describing the cost function is represented as an acyclic, directed graph where nodes with children are mathematical operators that have a defined derivative, such as multiplication, addition, reduce sum, and discrete Fourier transform while childless nodes are either variables or constants. Operator nodes take their children as arguments. The children of operators can be other operators, variables, and constants. Since the operators used are differentiable, the chain rule allows us to find the derivative of a node by calculating and combining the derivatives and values of its children in a process called Automatic Differentiation.

Complete gradients of the cost function are calculated with respect to each phase mask element and are updated using an optimization algorithm to minimize the value of the cost function. This representation is facilitated by the graph-based linear algebra library TensorFlow [63]. The phases are updated using the Adam optimizer [64].

Figures 7.2b and7.2c show optimized phase-masks for 1D-to-2D mapping. We impose a square aperture for the phase masks with dimension of $2\ mm \times 2\ mm$. The 1D SLM pixel pitch is $p = 25\ \mu m$.
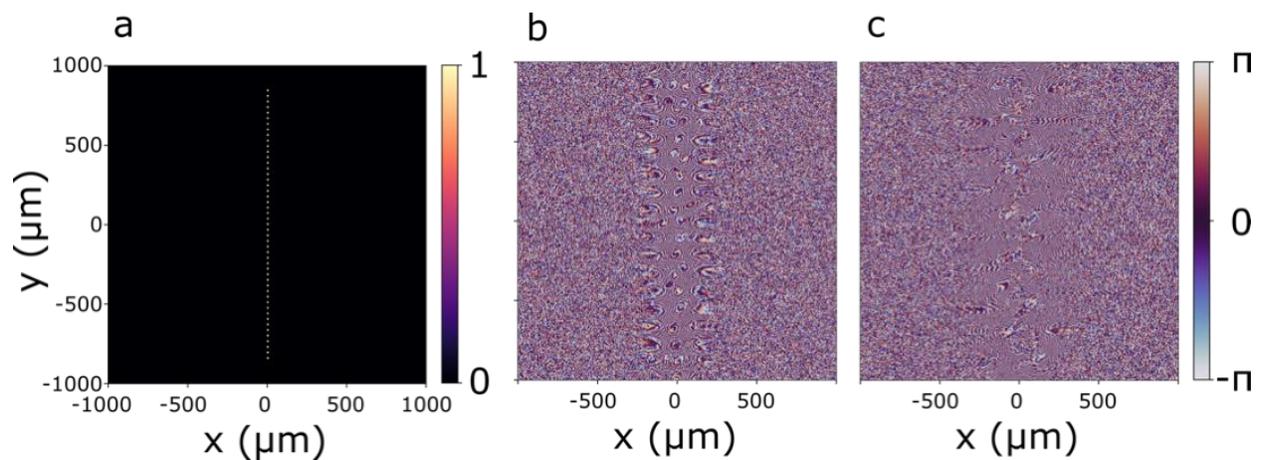
Figure 7.2. a) Input pixel intensity, optimized phase profiles for the a) first and b) second phase mask.

Using these phase masks, we can map a 1D array to a 2D field distribution. When excited by individual pixels from the 1D SLM, the output field at the 2D SLM output will be illuminated. The output fields are well defined within the output pixel boundary. It is important to note that the output modes demonstrated in this paper are just a single choice of basis and other more appropriate bases can be used depending on the application.
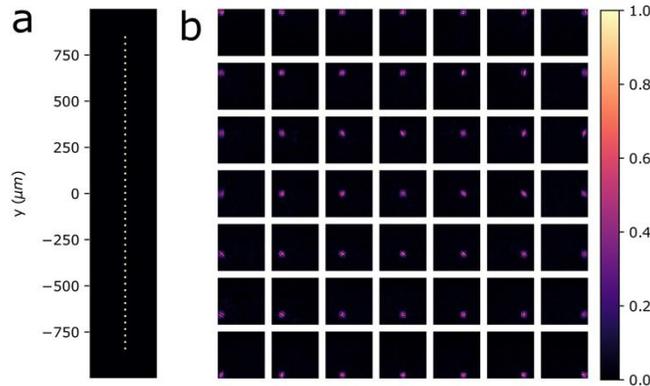
Figure 7.3. a) Input 49 element 1D SLM with all input pixels illuminated; b) Simulated output

modes for 1D 49 element SLM input.

Figure 7.3a shows the 1D array of 49 spots. Each spot maps to a specific point in the 2D plane, as shown in the 7×7 array in figure 7.3b, when passing through two phase-masks. The 49 points in the resulting 2D array will approximate a complete intensity basis in the 7×7 output space. The mean input-to-output power efficiency was 0.88 for all modes with a variance of 0.003. We note that the choice of 49 pixels is limited by the currently available computational resources in our team. More pixels can be added to increase the image resolution. We also emphasize that 1D SLMs with millions of pixels can be fabricated using current semiconductor technologies to the required resolution. However, the pitch of the input 1D SLM will eventually be limited by diffraction, as explained later.
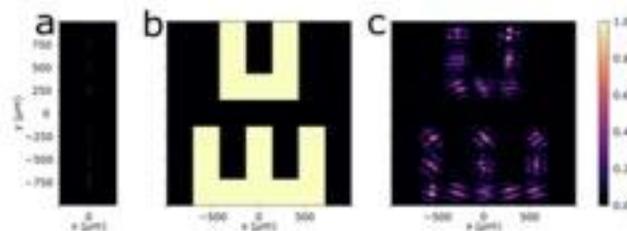
Figure 7.4. a) 1D SLM input field b) Target output field c) Simulated output field using 1D-to-

2D mapping

Illuminating appropriate pixels in the 1D array, arbitrary 2D patterns can be generated. Figure 4 shows the projection of such an arbitrary pattern: the letters "UW". We attribute the stripe-like features in the simulated output field to our choice of the cost-function: our cost function does not prioritize uniformity inside a pixel, and rather optimizes the total power in that pixel.
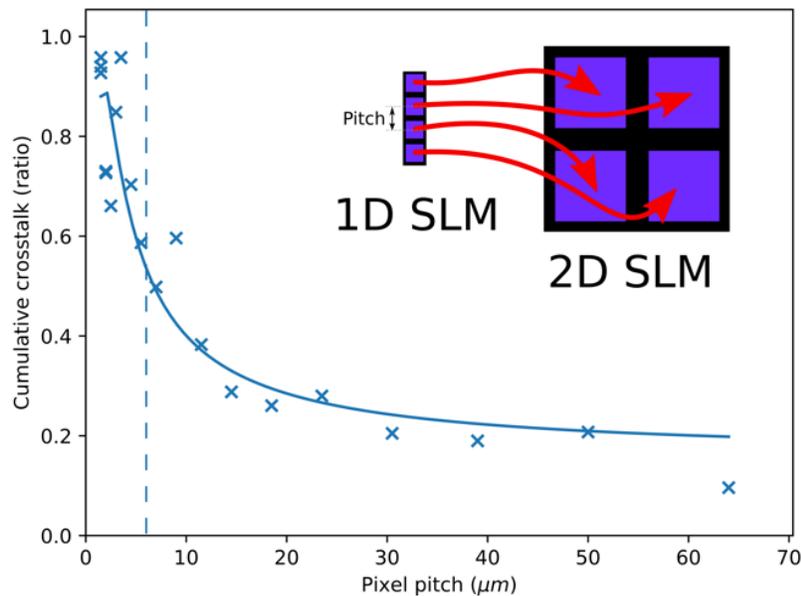
Figure 7.5. Cumulative crosstalk between output modes for a range of trained systems that map a 4-pixel 1D SLM to a 2×2 output SLM. The simulation region was shrunk by a factor of 10 to clearly observe the breakdown of our proposed method. All other simulation parameters are identical to the featured model except for the input pixel pitch. The solid curve serves as a guide to the eye.

Finally, we analyze how diffraction poses a limit on the proposed 1D-to-2D transformation. Light from different pixels in the 1D array impinges on the phase masks at different angles, and thus the reshaping of the 1D array to a 2D space fundamentally depends on the angular resolution of the phase-mask doublet. For the arrangements of the optics simulated here, the Abbe diffraction

limit dictates that two points in the 1D-SLM plane can be distinguished if their separation is greater than 633nm (presuming a circular aperture). We hypothesize that when the pixel pitch approaches this limit, our 1D-to-2D mapping starts to fail. To validate this hypothesis, we modify the simulation so that the grid pitch is near the diffraction limit, without incurring high computational cost and memory requirement. Specifically, we reduce the size of the apertures (e.g., diameter of the meta-optics and lateral size of the 1D-SLM) by a factor of 10 but keep the longitudinal distances the same. In this reduced simulation space, the Abbe diffraction limit becomes 6.33 μm, as only the aperture is scaled and not the longitudinal dimensions. Then, we optimize a set of identical systems (albeit with different pixel pitch in the 1D SLM) that map a 4 pixel, 1D SLM to a 2×2 2D pixel output and quantify the error as the cumulative crosstalk (Figure 5). A crosstalk of 1 indicates that energy from a single input pixel is distributed uniformly across all output pixels while a crosstalk of 0 means that all power is within the intended output pixel. This value is summed across all the inputs for a given simulation to calculate the cumulative crosstalk. As expected, the performance of the phase mask doublet markedly decreases as the input pixel separation approaches the diffraction limit (~6.33 μm). We note that, the tolerable value of the crosstalk will depend on the exact application. Additionally, we anticipate the crosstalk effect primarily coming from the neighboring pixels, and hence, the 2×2 simulation provides a good estimate of the crosstalk for larger arrays.

The proposed method could be experimentally verified with commercial SLMs, for example a grating light valve used by others [62]. In fact, the dimensions used in our simulations are motivated by experimental feasibility, such as the dimensions of the beam expanders and spacing between optics. The phase masks can be implemented using meta-optics [26]. Meta-optics are subwavelength diffractive optics that can shape the phase of incident light with high spatial

resolution [37], [38]. Sub-wavelength optical scatterers are spatially arranged in a meta-optics to provide spatially varying phase shifts to the incident optical wavefront [45], [65]–[67]. The phasor response of the phase mask elements can be simulated using a rigorous full wave electromagnetic simulation, such as finite-difference time-domain or rigorous coupled-wave analysis [25], [38]. Under local phase approximation (assuming the neighboring scatterers have minimal coupling), individual scatterers are placed where their phase delay matches the desired phase delay of the phase mask. The doublet can be realized by fabricating two meta-optics on both sides of a glass slide [68]. Additionally, mm-aperture, visible wavelength metasurfaces have already been reported and can potentially be scaled to even larger apertures [69].

In summary, we propose a method to generate arbitrary 2D intensity profiles from a 1D SLM using a pair of inverse-designed meta-optics. We validate our design via numerical simulation and explore how diffraction limits such mapping. Our proposed method can potentially alleviate the routing challenges for sub-wavelength SLMs, enabling a high-speed modulation of 2D optical modes.

8. Concluding remarks

Meta-optics have shown great potential in many fields including image, optical cavities, general purpose optics and computation. They show promise in existing optical fields and allow for novel devices to be created. This thesis represents my work throughout my research in my PhD on the subjects of electronically and physical tunable meta-optics.

This work began by describing what meta-optics are, the current state and potential application of metasurface optics, and why meta-optics is such a promising field. To summarize, meta-optics are sub-wavelength diffractive optics with potential to displace certain conventional refractive and diffractive optics while some providing some novel solutions. Metasurfaces are a special case of diffractive optics which are made up of scatterers that are placed on a period that is small enough to not have any non-zero order diffraction. They can be manufactured with processes used in the mature semi-conductor manufacturing industry and therefore can be easily scalable. The scatterer design can be tailored to independently control wavelength and polarization response and can produce free-form and computational optics. However, the metasurface scatterers are limited in terms of efficiency and can suffer from large chromatic dispersion.

The design of meta-optics was then explored. It was described how a phase profile could be implemented placing simulated optical scatterers in an arrangement that corresponded to the desired phase response. The generalized diffraction equation sets an upper bound for scatterer period to avoid non-zero diffraction orders depending on wavelength, incident angle, and refractive indices or the materials involved. The generalized Snell's law dictates how a phase gradient will affect the refraction angle at an interface. These two equations govern the design of phase gradient metasurfaces.

Then, the fabrication methods for dielectric, visible metasurfaces using the silicon nitride material platform was shown. Using standard processes developed for the semi-conductor industry, silicon nitride scatterers can be fabricated to create visible wavelength metasurfaces. These processes include rapid silicon nitride material deposition using plasma assisted chemical reactions that precipitate reaction products on a wafer. This is followed by electron beam lithography to define the structures and dry etch steps involving the reaction between the exposed silicon nitride and plasma activated reactants to form volatile reaction products.

The design of a simple hyperbolic meta-lens using forward design was shown. Also, methods to model the propagation of light after interacting with the metasurface were explored. This method is instrumental in modeling the propagation of light over large distances in free space and the inverse design of phase profiles.

Next, design and experimental demonstration of digital tuning was shown. Here, computational techniques were used to extract data from various planes of an extended depth of focus optics. This showcased the flexibility of meta-optics to manifest arbitrary phase profiles, allowing for arbitrary phase mask to create depth invariant focal spots. The computational techniques effectively allowed for variable focal length modulation allowing for practical camera systems that are more versatile. This work would hopefully lead to scalable production of extended depth of focus optics which would enhance the capabilities of imaging technology.

To expand on the digital tuning project, physical tuning methods from an electro-optic polymer was explored. A 1D meta-optic cavity was designed to create 1D spatial variation. This physical tuning mechanism shows potential for high-speed tunable meta-optic that can enhance the functionality of active optical systems. A higher speed 1D spatial light modulator would enhance many optical systems such a non-line of slight imaging and virtual/augmented reality.

Finally, using models that propagate light through space and perform gradient-based optimization on the model, the design of complex optical operation was shown. 1D arrangements of source modes were mapped into a 2D arrangements of output modes, demonstrating the design methods for general metasurface inverse design. This multilayer inverse design method could be applied for general optimization of optical systems.

9. References

[1] J. P. Rolland et al., "Freeform optics for imaging," Optica, vol. 8, no. 2, pp. 161–176, Feb. 2021, doi: 10.1364/OPTICA.413762.

[2] Zhan Alan, Gibson Ricky, Whitehead James, Smith Evan, Hendrickson Joshua R., and Majumdar Arka, "Controlling three-dimensional optical fields via inverse Mie scattering," Science Advances, vol. 5, no. 10, p. eaax4769, doi: 10.1126/sciadv.aax4769.

[3] A. F. J. Levi, Essential Classical Mechanics for Device Physics. Morgan & Claypool Publishers, 2016. doi: 10.1088/978-1-6817-4413-1.

[4] S. Colburn et al., "Broadband transparent and CMOS-compatible flat optics with silicon nitride metasurfaces [Invited]," Opt. Mater. Express, vol. 8, no. 8, pp. 2330–2344, Aug. 2018, doi: 10.1364/OME.8.002330.

[5] N. A. Rubin, Z. Shi, and F. Capasso, "Polarization in diffractive optics and metasurfaces," Adv. Opt. Photon., vol. 13, no. 4, pp. 836–970, Dec. 2021, doi: 10.1364/AOP.439986.

[6] W. Ye et al., "Spin and wavelength multiplexed nonlinear metasurface holography," Nature Communications, vol. 7, no. 1, p. 11930, Jun. 2016, doi: 10.1038/ncomms11930.

[7] E. Arbabi, S. M. Kamali, A. Arbabi, and A. Faraon, "Full-Stokes Imaging Polarimetry Using Dielectric Metasurfaces," ACS Photonics, vol. 5, no. 8, pp. 3132–3140, Aug. 2018, doi: 10.1021/acsphotonics.8b00362.

[8] Y.-Y. Xie et al., "Metasurface-integrated vertical cavity surface-emitting lasers for programmable directional lasing emissions," Nature Nanotechnology, vol. 15, no. 2, pp. 125–130, Feb. 2020, doi: 10.1038/s41565-019-0611-y.

[9]   X. He, Y. Liu, P. Beckett, H. Uddin, A. Nirmalathas, and R. R. Unnithan, "CMY camera using a nanorod filter mosaic integrated on a CMOS image sensor," OSA Continuum, vol. 4, no. 1, pp. 229–238, Jan. 2021, doi: 10.1364/OSAC.413709.

[10] S. Colburn, A. Zhan, and A. Majumdar, "Metasurface optics for full-color computational imaging," Sci Adv, vol. 4, no. 2, p. eaar2114, Feb. 2018, doi: 10.1126/sciadv.aar2114.

[11] Z. Han, S. Colburn, A. Majumdar, and K. F. Böhringer, "MEMS-actuated metasurface Alvarez lens," Microsystems & Nanoengineering, vol. 6, no. 1, p. 79, Oct. 2020, doi: 10.1038/s41378-020-00190-6.

[12] Z. Han, S. Colburn, A. Majumdar, and K. F. Bohringer, "Millimeter-scale focal length tuning with MEMS-integrated meta-optics employing high-throughput fabrication." 2021.

[13] E. Arbabi, A. Arbabi, S. M. Kamali, Y. Horie, M. Faraji-Dana, and A. Faraon, "MEMS-tunable dielectric metasurface lens," Nature Communications, vol. 9, no. 1, p. 812, Feb. 2018, doi: 10.1038/s41467-018-03155-6.

[14] G. Zheng, H. Mühlenbernd, M. Kenney, G. Li, T. Zentgraf, and S. Zhang, "Metasurface holograms reaching 80% efficiency," Nature Nanotechnology, vol. 10, no. 4, pp. 308–312, Apr. 2015, doi: 10.1038/nnano.2015.2.

[15] Y. Zhu et al., "High-efficiency all-silicon metasurfaces with 2π phase control based on multiple resonators," Results in Physics, vol. 29, p. 104765, Oct. 2021, doi: 10.1016/j.rinp.2021.104765.

[16] E. Arbabi, A. Arbabi, S. M. Kamali, Y. Horie, and A. Faraon, "Controlling the sign of chromatic dispersion in diffractive optics with dielectric metasurfaces," Optica, vol. 4, no. 6, pp. 625–632, Jun. 2017, doi: 10.1364/OPTICA.4.000625.

[17] W. T. Chen, A. Y. Zhu, and F. Capasso, "Flat optics with dispersion-engineered metasurfaces," Nature Reviews Materials, vol. 5, no. 8, pp. 604–620, Aug. 2020, doi: 10.1038/s41578-020-0203-3.

[18] S. W. Hell and J. Wichmann, "Breaking the diffraction resolution limit by stimulated emission: stimulated-emission-depletion fluorescence microscopy," Opt. Lett., vol. 19, no. 11, pp. 780–782, Jun. 1994, doi: 10.1364/OL.19.000780.

[19] E. G. Loewen and E. Popov, Diffraction Gratings and Applications. Taylor & Francis, 1997. [Online]. Available: https://books.google.com/books?id=IlMBiFGO4pMC

[20] Yu Nanfang et al., "Light Propagation with Phase Discontinuities: Generalized Laws of Reflection and Refraction," Science, vol. 334, no. 6054, pp. 333–337, Oct. 2011, doi: 10.1126/science.1210713.

[21] N. Meinzer, W. L. Barnes, and I. R. Hooper, "Plasmonic meta-atoms and metasurfaces," Nature Photonics, vol. 8, no. 12, pp. 889–898, Dec. 2014, doi: 10.1038/nphoton.2014.247.

[22] J. E. M. Whitehead, A. Zhan, S. Colburn, L. Huang, and A. Majumdar, "Fast extended depth of focus meta-optics for varifocal functionality," Photon. Res., vol. 10, no. 3, pp. 828–833, Mar. 2022, doi: 10.1364/PRJ.434681.

[23] M. Albooyeh et al., "Resonant metasurfaces at oblique incidence: interplay of order and disorder," Scientific Reports, vol. 4, no. 1, p. 4484, Mar. 2014, doi: 10.1038/srep04484.

[24] A. F. Oskooi, D. Roundy, M. Ibanescu, P. Bermel, J. D. Joannopoulos, and S. G. Johnson, "MEEP: A flexible free-software package for electromagnetic simulations by the FDTD method," Computer Physics Communications, vol. 181, pp. 687–702, Jan. 2010, doi: 10.1016/j.cpc.2009.11.008.

[25] V. Liu and S. Fan, "S4 : A free electromagnetic solver for layered periodic structures," Computer Physics Communications, vol. 183, no. 10, pp. 2233–2244, 2012, doi: https://doi.org/10.1016/j.cpc.2012.04.026.

[26] A. Zhan, S. Colburn, C. M. Dodson, and A. Majumdar, "Metasurface Freeform Nanophotonics," Scientific Reports, vol. 7, no. 1, p. 1673, May 2017, doi: 10.1038/s41598-017-01908-9.

[27] X. Lin et al., "All-optical machine learning using diffractive deep neural networks," Science, vol. 361, no. 6406, p. 1004, Sep. 2018, doi: 10.1126/science.aat8084.

[28] L. Hsu, M. Dupré, A. Ndao, J. Yellowhair, and B. Kanté, "Local phase method for designing and optimizing metasurface devices," Opt. Express, vol. 25, no. 21, pp. 24974–24982, Oct. 2017, doi: 10.1364/OE.25.024974.

[29] M. V. Zhelyeznyakov, S. Brunton, and A. Majumdar, "Deep Learning to Accelerate Scatterer-to-Field Mapping for Inverse Design of Dielectric Metasurfaces," ACS Photonics, vol. 8, no. 2, pp. 481–488, Feb. 2021, doi: 10.1021/acsphotonics.0c01468.

[30] J. W. Goodman, Introduction to Fourier Optics. W. H. Freeman, 2005. [Online]. Available: https://books.google.com/books?id=ow5xs_Rtt9AC

[31] K. Matsushima and T. Shimobaba, "Band-Limited Angular Spectrum Method for Numerical Simulation of Free-Space Propagation in Far and Near Fields," Opt. Express, vol. 17, no. 22, pp. 19662–19673, Oct. 2009, doi: 10.1364/OE.17.019662.

[32] S. W. Seo et al., "Microelectromechanical-System-Based Variable-Focus Liquid Lens for Capsule Endoscopes," Japanese Journal of Applied Physics, vol. 48, no. 5, p. 052404, May 2009, doi: 10.1143/jjap.48.052404.

[33] E. R. Dowski and W. T. Cathey, "Extended depth of field through wave-front coding," Appl. Opt., vol. 34, no. 11, pp. 1859–1866, Apr. 1995, doi: 10.1364/AO.34.001859.

[34] Zeev Zalevsky, "Extended depth of focus imaging: a review," SPIE Reviews, vol. 1, no. 1, pp. 1–11, Jan. 2010, doi: 10.1117/6.0000001.

[35] Rocha Karolinne Maia, "Extended Depth of Focus IOLs: The Next Chapter in Refractive Technology?," Journal of Refractive Surgery, vol. 33, no. 3, pp. 146–149, Mar. 2017, doi: 10.3928/1081597X-20170217-01.

[36] S. Banerji, M. Meem, A. Majumder, B. Sensale-Rodriguez, and R. Menon, "Extreme-depth-of-focus imaging with a flat lens," Optica, vol. 7, no. 3, pp. 214–217, Mar. 2020, doi: 10.1364/OPTICA.384164.

[37] S. M. Kamali, E. Arbabi, A. Arbabi, and A. Faraon, "A review of dielectric optical metasurfaces for wavefront control," Nanophotonics, vol. 7, no. 6, pp. 1041–1068, Jun. 2018, doi: https://doi.org/10.1515/nanoph-2017-0129.

[38] A. Zhan, S. Colburn, R. Trivedi, T. K. Fryett, C. M. Dodson, and A. Majumdar, "Low-Contrast Dielectric Metasurface Optics," ACS Photonics, vol. 3, no. 2, pp. 209–214, Feb. 2016, doi: 10.1021/acsphotonics.5b00660.

[39] L. Huang, J. Whitehead, S. Colburn, and A. Majumdar, "Design and analysis of extended depth of focus metalenses for achromatic computational imaging," Photon. Res., vol. 8, no. 10, pp. 1613–1623, Oct. 2020, doi: 10.1364/PRJ.396839.

[40] E. Bayati, R. Pestourie, S. Colburn, Z. Lin, S. G. Johnson, and A. Majumdar, Inverse Designed Extended Depth of Focus Meta-Optics for Broadband Imaging in the Visible. 2021.

[41] R. Pestourie, C. Pérez-Arancibia, Z. Lin, W. Shin, F. Capasso, and S. G. Johnson, "Inverse design of large-area metasurfaces," Opt. Express, vol. 26, no. 26, pp. 33732–33747, Dec. 2018, doi: 10.1364/OE.26.033732.

[42] E. Tseng et al., Neural Nano-Optics for High-quality Thin Lens Imaging. 2021.

[43] U. Akpinar, E. Sahin, M. Meem, R. Menon, and A. Gotchev, Learning Wavefront Coding for Extended Depth of Field Imaging. 2020.

[44] P. Getreuer, "Total Variation Deconvolution using Split Bregman," Image Processing On Line, 2012, doi: 10.5201/ipol.2012.g-tvdc.

[45] E. Tseng et al., Neural Nano-Optics for High-quality Thin Lens Imaging. 2021.

[46] "LIQUID LENSES IN MACHINE VISION." Edmund Optics. [Online]. Available: https://www.edmundoptics.com/ViewDocument/EO_Liquid_Lenses_in_Machine_vision_0 419_EN.pdf

[47] B. Forster, D. Van De Ville, J. Berent, D. Sage, and M. Unser, "Complex wavelets for extended depth-of-field: a new method for the fusion of multichannel microscopy images.," Microsc Res Tech, vol. 65, no. 1–2, pp. 33–42, Sep. 2004, doi: 10.1002/jemt.20092.

[48] F. Aguet, D. Van De Ville, and M. Unser, "Model-based 2.5-d deconvolution for extended depth of field in brightfield microscopy.," IEEE Trans Image Process, vol. 17, no. 7, pp. 1144–1153, Jul. 2008, doi: 10.1109/TIP.2008.924393.

[49] M. Abadi et al., "TensorFlow: Large-Scale Machine Learning on Heterogeneous Distributed Systems." arXiv, 2016. doi: 10.48550/ARXIV.1603.04467.

[50] A. Paszke et al., "PyTorch: An Imperative Style, High-Performance Deep Learning Library." arXiv, 2019. doi: 10.48550/ARXIV.1912.01703.

[51] C. Kieninger et al., "Ultra-high electro-optic activity demonstrated in a silicon-organic hybrid modulator," Optica, vol. 5, no. 6, pp. 739–748, Jun. 2018, doi: 10.1364/OPTICA.5.000739.

[52] M. Faraji-Dana, E. Arbabi, A. Arbabi, S. M. Kamali, H. Kwon, and A. Faraon, "Compact folded metasurface spectrometer," Nature Communications, vol. 9, no. 1, p. 4196, Oct. 2018, doi: 10.1038/s41467-018-06495-5.

[53] G. W. Y. Peng S. Choi, N. Padmanaban, "Neural Holography with Camera-in-the-loop Training," ACM Trans. Graph. (SIGGRAPH Asia), 2020.

[54] D. Faccio, "Non-Line-of-Sight Imaging," Opt. Photon. News, vol. 30, no. 1, pp. 36–43, Jan. 2019, doi: 10.1364/OPN.30.1.000036.

[55] A. Ryou et al., Free-space optical neural network based on thermal atomic nonlinearity. 2021.

[56] A. P. Mosk, A. Lagendijk, G. Lerosey, and M. Fink, "Controlling waves in space and time for imaging and focusing in complex media," Nature Photonics, vol. 6, no. 5, pp. 283–292, May 2012, doi: 10.1038/nphoton.2012.88.

[57] J. Park et al., "All-solid-state spatial light modulator with independent phase and amplitude control for three-dimensional LiDAR applications," Nature Nanotechnology, Oct. 2020, doi: 10.1038/s41565-020-00787-y.

[58] A. Karvounis, V. V. Vogler-Neuling, F. U. Richter, E. Dénervaud, M. Timofeeva, and R. Grange, "Electro-Optic Metasurfaces Based on Barium Titanate Nanoparticle Films," Advanced Optical Materials, vol. 8, no. 17, p. 2000623, 2020, doi: 10.1002/adom.202000623.

[59] K. Liu, S. Sun, A. Majumdar, and V. J. Sorger, "Fundamental Scaling Laws in Nanophotonics," Scientific Reports, vol. 6, no. 1, p. 37419, Nov. 2016, doi: 10.1038/srep37419.

[60] B. J. Lechner, F. J. Marlowe, E. O. Nester, and J. Tults, "Liquid crystal matrix displays," Proceedings of the IEEE, vol. 59, no. 11, pp. 1566–1579, Nov. 1971, doi: 10.1109/PROC.1971.8489.

[61] G. K. Shirmanesh, R. Sokhoyan, P. C. Wu, and H. A. Atwater, "Electro-optically Tunable Multifunctional Metasurfaces," ACS Nano, vol. 14, no. 6, pp. 6912–6920, Jun. 2020, doi: 10.1021/acsnano.0c01269.

[62] O. Tzang, E. Niv, S. Singh, S. Labouesse, G. Myatt, and R. Piestun, "Wavefront shaping in complex media with a 350 kHz modulator via a 1D-to-2D transform," Nature Photonics, vol. 13, no. 11, pp. 788–793, Nov. 2019, doi: 10.1038/s41566-019-0503-6.

[63] Martín Abadi et al., TensorFlow: Large-Scale Machine Learning on Heterogeneous Systems. 2015. [Online]. Available: http://tensorflow.org/

[64] D. P. Kingma and J. Ba, Adam: A Method for Stochastic Optimization. 2017.

[65] H. Kwon, E. Arbabi, S. M. Kamali, M. Faraji-Dana, and A. Faraon, "Single-shot quantitative phase gradient microscopy using a system of multifunctional metasurfaces," Nature Photonics, vol. 14, no. 2, pp. 109–114, Feb. 2020, doi: 10.1038/s41566-019-0536-x.

[66] D. Lin, P. Fan, E. Hasman, and M. L. Brongersma, "Dielectric gradient metasurface optical elements," Science, vol. 345, no. 6194, pp. 298–302, 2014, doi: 10.1126/science.1253213.

[67] N. Yu and F. Capasso, "Flat optics with designer metasurfaces," Nature Materials, vol. 13, no. 2, pp. 139–150, Feb. 2014, doi: 10.1038/nmat3839.

[68] A. Arbabi, E. Arbabi, S. M. Kamali, Y. Horie, S. Han, and A. Faraon, "Miniature optical planar camera based on a wide-angle metasurface doublet corrected for monochromatic aberrations," Nature Communications, vol. 7, no. 1, p. 13682, Nov. 2016, doi: 10.1038/ncomms13682.

[69] S. Colburn, A. Zhan, and A. Majumdar, "Varifocal zoom imaging with large area focal length adjustable metalenses," Optica, vol. 5, no. 7, pp. 825–831, Jul. 2018, doi: 10.1364/OPTICA.5.000825.

10. ACKNOWLEDGMENTS